Internal degrees of freedom in membranes and synchronization phenomena at low Reynolds number

by

Hongyuan Jiang

M.Sc. in Applied Mathematics, Brown University, May 2009.

M.Sc. in Mechanical Engineering, Brown University, May 2006.

A dissertation submitted in partial fulfillment of the

requirements for the degree of Doctor of Philosophy

in the Division of Engineering at Brown University

PROVIDENCE, RHODE ISLAND

May 2010

Abstract of "Internal degrees of freedom in membranes and synchronization phenomena at low Reynolds number" by Hongyuan Jiang, Ph.D., Brown University, May 2010

The cell membrane is not a simple assembly of lipids and proteins. There are many internal degrees of freedom in a membrane, such as the shape of lipid molecules, the tilt direction of lipid molecules and the species of lipids and proteins in a biological membrane. Here we study two different internal degrees of freedom in membranes and their effects on the cell morphology and biological processes. Motivated by the propensity for tilt order and the common occurrence of narrow necks in the intermediate stages of biological processes such as endocytosis and vesicle trafficking, we examine how tilt order inhibits the formation of necks in the equilibrium shapes. In addition, motivated by recent experiments which showed that the mechanical properties of membranes play an important role in lipid sorting, a model is developed to study how the coupling between membrane composition and membrane bending stiffness and tension affects tubule formation in a multi-component membrane. We show that drawing a tubule from a vesicle leads to a rearrangement of composition in which the phase of higher flexibility segregates into the highly curved tubule. Lastly, this thesis will also study the synchronization of cilia and flagella. Motivated by the observed coordination of nearby beating cilia, we use a scale model experiment to show that hydrodynamic interactions can cause synchronization between rotating paddles driven at constant torque in a very viscous fluid. Synchronization is only observed when the shafts supporting the paddles have some flexibility. The phase difference in the synchronized state depends on the symmetry of the paddles. Calculations using the method of regularized stokeslets and analytic theory match the experimental observations well.

This dissertation by Hongyuan Jiang is accepted in its present form

by the Division of Engineering as satisfying the

dissertation requirement for the degree of Doctor of Philosophy.

Date_____

_____

Thomas R. Powers, Ph.D., Advisor

Recommended to the Graduate Council

Date_____

_____

Jay X. Tang, Ph.D., Reader

Date_____

_____

Vivek Shenoy, Ph.D., Reader

Approved by the Graduate Council

Date_____

_____

Sheila Bonde, Dean of the Graduate School

The Vita of Hongyuan Jiang

Hongyuan Jiang was born in 1979, at Mishan, Heilongjiang, P. R. China. In 1997, he attended University of Science and Technology of China where he received his Bachelor degree in Mechanical Engineering in 2001 and Master degree in solid mechanics in 2004. Then he joined the Solid Mechanics group at Brown University in the fall of 2004. He received Masters degree in Solid Mechanics in 2006 and Masters degree in Applied Mathematics in 2009.

Acknowledgments

I would like to express my deep and tremendous thanks to my advisor, Professor Thomas R. Powers for his guidance, support, and patience. He taught me to do research strictly and independently. He also gave me a lot of freedom to explore what I'm interested in.

I want to deeply thank Professor Greg Huber, Robert A. Pelcovits and Kenneth S. Breuer. I benefited a lot from the collaboration and discussion with them. My thanks also go to Bian Qian, who did the excellent experiments.

I also want to thank my fellows and friends Jin Qian, Xinghua Shi, Wendong Shi, Yi Dong, Xiaoyan Li, Peng Chen, Ningning Du, Yuan Lin, Yujie Wei, Fang Zhang, Lei Li, Chao Wang and Menghan Wang for their support and help in my graduate study.

Lastly, I want to thank my parents and my sister. Their supports and understandings made the accomplishment of this work possible.

Contents

List of Figures

Chapter 1

Introduction

In this thesis I focus on internal degrees of freedom in membranes, and synchronization phenomena at low Reynolds number. We begin with an fundamental introduction to the basic facts of membranes, cilia and flagella.

The cell membrane, which is also called the plasma membrane or phospholipid bilayer, is an interface between the intracellular components and the extracellular fluid environment [1]. The cell membranes not only define the boundary of cell, but also play important roles in lipid and protein traffic, cell adhesion, ion channel and cell signaling. The cell membrane is primarily built from amphiphilic molecules, such as phospholipids, glycolipids, and steroids. Usually, amphiphilic molecules have a hydrophilic head and two hydrophobic tails. They can self-organize to form the membrane bilayer so that the hydrophobic tails are shielded from the surrounding polar fluid by the hydrophilic head.

All lipids have a transition temperature [22]. Below this temperature, the membrane is in a gel (solid) phase. Above this temperature, the membrane is in a fluid phase. In the fluid phase, the lipids can diffuse freely in the bilayer. The diffusion constant is as fast

as $1\,\mu\mathrm{m}^2/\mathrm{s}$. Unlike the fluid phase, the lipids in the gel phase tilt relative to the surface normal. So the gel phase bilayer is anisotropic and there could exist a quasi-long range orientational order.

The cell membrane contains many species of lipids and proteins. The aggregate of these lipids and proteins exhibits a lot of interesting behaviors. For example, in vitro experiments using dioleylphosphatidylcholine (DOPC), cholesterol (Chol) and sphingomyelin (SM), the mixture of lipids can separate into lipid order (L_o) phase and lipid disorder (L_d) phase [7, 2, 40]. The composition of lipids is different in each phase. Cholesterol and sphingomyelin are enriched in the liquid ordered phase, and DOPC prefers the liquid disordered phase. The difference in composition results in the difference of the mechanical properties of the L_o and L_d phases. The bending stiffness of the L_o phase is about twice that of the L_d phase [2]. The microdomain of the cholesterol-enriched (L_o) phase is also referred to as a lipid raft. Lipid rafts are the essential structure in lipid or protein traffic, endocytosis and exocytosis [64]. Lipid rafts also play an important role in cellular signal transduction [44]. Certain proteins associated with signalling processes tend to be present in the lipid rafts, while other proteins are excluded from the lipid rafts.

The morphology of a fluid membrane (in fluid phase) is mainly determined by its bending stiffness. The vesicle shape for the fluid membrane is well studied [19, 79, 77]. But the shape transformations of a membrane with tilt order (in gel phase) are still not clear. The bending stiffness of the membrane is about tens k_BT for phospholipid. The interaction energy of tilted molecules is of the same magnitude as the bending energy. So the effect of tilted molecules is not negligible. The membrane morphology for tilt membrane is not only determined by bending energy, but also influenced by the interaction energy of

tilted molecules.

For a multi-component membrane, the morphology is even more complicated since the bending stiffness is distinct for the L_o and L_d phase. In this case, the curvature of the membrane and the composition of the lipids are coupled together. The soft phase tends to aggregate into the high curvature region to reduce the bending energy of the membrane, which can change the membrane morphology dramatically. The rearrangement of lipids also suggests that the mechanical properties of lipids could be a very important criteria for lipid sorting and traffic in real biological system. We will discuss how the tilt order affects the vesicle shape and how the lipids are sorted and located according to the bending stiffness of the L_o and L_d phase in Chapter 2 [32] and chapter 3 [41] respectively.

This thesis will also study the synchronization of cilia and flagella. Synchronization is a very common and interesting phenomenon in our day life. For example, thousands of Asian fireflies are able to blink altogether without a commander firefly. The applause by audience can synchronize several times during a concert [93]. Huygens, the inventor of pendulum clock, found two pendulums will always end up swinging in exactly opposite directions, when suspended together on the same beam. Researchers believe the synchronization comes from the imperceptible movement of the beam [8].

Another example of synchronization in biological system is the coordination of cilia and flagella. Cilia and flagella are hair-like projections from the cell body. They have the same internal structure. The major difference is in their length. Cilia extend approximately $5--10$ micrometers. Flagella are much longer. The primary function of cilia and flagella is to propel the cell itself or to move fluid, food or even other cells over their surface. Due to their small length scale, the motion of cilia and flagella can be described by the

fluid mechanics at low Reynolds number. The mechanism of the synchronization of cilia and flagella is still not quite clear. In Chapter 4, We set up a tabletop experiment using two rectangular paddles driven by constant torque in a viscous fluid. The goal is to understand how hydrodynamic interactions lead the paddles to synchronize. The results are compared with the simulation with regularized Stokeslet method [14]. In Chapter 5, we set up a simple model to describe the synchronization phenomena at low Reynolds number. Analytical solutions are obtained and compared with simulation for both asymmetric and symmetric configurations.

The work in Chapter 3 [41] was carried out with Thomas R. Powers. The work in Chapter 2 [32] was a collaboration with Greg Huber, Robert A. Pelcovits and Thomas R. Powers. Qian Bian and Kenneth S. Breuer performed the experiments in Chapter 4 [6].

Chapter 2

Vesicle shape, molecular tilt, and the suppression of necks

2.1 Introduction

Can the presence of molecular-tilt order significantly affect the shapes of lipid bilayer membranes, particularly membrane shapes with narrow necks? Motivated by the propensity for tilt order and the common occurrence of narrow necks in the intermediate stages of biological processes such as endocytosis and vesicle trafficking, we examine how tilt order inhibits the formation of necks in the equilibrium shapes of vesicles in this chapter.

The interplay of surface curvature and liquid-crystalline order finds its fullest expression in the manifold and complex biological realizations of the bilayer membranes surrounding cells and intracellular organelles. Helfrich [34] was one of the first to connect membrane shape and molecular order, by realizing that the spontaneous curvature of a bilayer membrane could arise from the spontaneous splay of the ordered rod-like lipid molecules com-

prising the membrane. But the biological world offers richer varieties of orientational order and shape that remain to be understood. For example, lipid molecules typically tilt relative to the normal of the membrane [83, 84, 63], and it has recently become possible to image tilt-ordered domains on the surface of curved, micron-scale membranes [94]. Furthermore, curvature has proven to play an active role in cellular and subcellular processes [60]. Narrow necks with small mean curvature but large negative Gaussian curvature are relevant to biological membranes that compartmentalize through budding, since this neck geometry allows separate membrane-bound compartments to be budded off, while avoiding high-energy membrane shapes. Neck formation is universal and crucial to the phenomena of endo- and exocytosis [26, 7], viral entry and budding, the traffic of continual fusion and fission of vesicle and Golgi membrane, and the interconnections between Golgi stacks [18] and between the smooth and rough endoplasmic reticulum. Because of the close association of these phenomena with cell function, it is crucial to understand the forces on membrane necks and the constraints on their formation.

In this paper we numerically calculate the equilibrium shapes of axisymmetric vesicles with tilt order. Figure 2.1 shows how dramatic the effect of tilt can be. The two vesicles have the same resistance to bending, the same enclosed volume, and the same area, but the one on the right has tilt order whereas the one on the left has no tilt order. As we review below, the tilt order may be described by a vector field which is tangent to the vesicle surface. Molecular interactions prefer uniform tilt order, which may be realized on a surface with zero Gaussian curvature such as a plane or the surface of a cylinder. But it is impossible to have a uniform vector field on a surface with nonzero Gaussian curvature, such as a sphere or the neck connecting the two spheres. Therefore, uniform

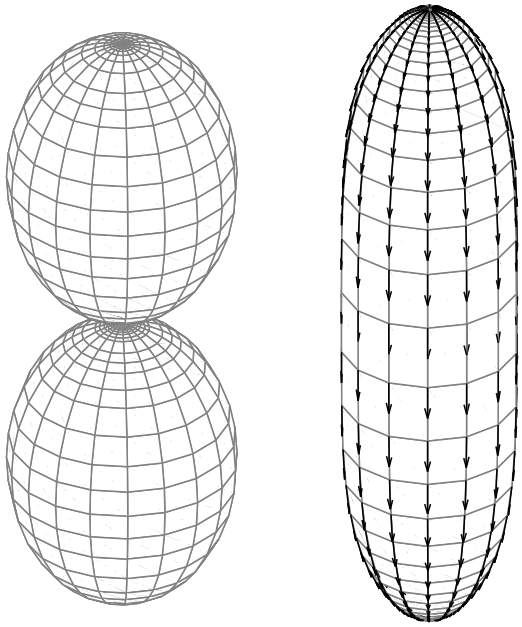

Figure 2.1: Effect of tilt order on membrane shape. Left: fluid membrane with reduced volume $v = 0.706$ and spontaneous curvature $c_0 = 2.4/R_0$, where R_0 is an overall length scale defined in Sec. 2.3. Right: Tilt-ordered membrane with same parameters and tilt modulus $K_m = 2.0\kappa$, where κ is the bending stiffness of the membrane. The arrows represent the tilt order. A +1 defect sits at both the north and the south poles of the vesicle.

molecular order and Gaussian curvature are incompatible [59, 57]. In particular, as long as the molecular interactions are strong enough, the elongated prolate shape of Fig. 2.1 will be preferred over a shape with a neck.

We begin with a brief discussion of the relation of our work to previous work on membrane shapes and orientational order. Section 2.3 describes our minimal isotropic tilt model, coordinates, and numerical method. Our analysis and methods are straightforward, but we describe them here to make our paper self-contained. In Sec. 2.4 we present the main results, which are the energy as a function of reduced volume for several different branches of solutions, and phase diagrams for shapes. In the final section we discuss the

implications and limitations of our analysis.

2.2 Relation to previous work

The equilibrium shapes of closed fluid membrane vesicles have been studied theoretically and experimentally for many years (see [78, 19], and references therein). In the spontaneous-curvature model pioneered by Helfrich, a patch of membrane has a resistance to bending but is curved in the absence of external loads [34]. A different approach known as the bilayer-coupling model accounts for the bilayer structure of a membrane by imposing a constraint on the number of molecules in both monolayers [86, 87]. Both models predict the same set of vesicle shapes. However, the spontaneous-curvature model predicts that most shape transitions are discontinuous, while the bilayer-coupling model predicts continuous transitions [79]. To simplify our discussion, we will consider the spontaneous-curvature model with tilt order.

As alluded to above, the basic physics governing the interaction of vesicle shape and orientational order is the incompatibility of Gaussian curvature and uniform order. This incompatibility is a local property: a patch of surface with Gaussian curvature cannot have uniform tilt order. The global topology of surfaces also constrains the number and strength of point defects in the orientation order field, via the Poincáre-Brouwer theorem, which states that the total defect strength of a vector field on a surface is equal to the Euler characteristic (see [45] for an elementary proof). In our problem, a point defect is an isolated point where the tilt order vanishes, and the strength of the defect is the number of rotations of the tilt order field around that point. For a vesicle with the topology of a

sphere, the total defect strength is +2. It is natural to suppose that the lowest energy states have two +1 defects at antipodal points (we shall impose this two-defect configuration).

MacKintosh and Lubensky modeled a vesicle with spherical topology made up of molecules undergoing a transition from an untilted smectic-A phase to a tilted smectic-C phase [59]. They found that an initially spherical vesicle elongates into a prolate shape, with most of the Gaussian curvature concentrated near the defects that form at the two poles. They calculated the change in shape for this transition assuming fixed area, but they did not constrain the enclosed volume. Other work has examined the transitions among spherical, cylindrical, and toroidal vesicles with orientational order, again without the constraint of fixed enclosed volume [57, 24]. In the current work, we impose the more realistic double constraint of fixed volume and fixed area, and solve for the shape. Also, our numerical method allows us to study shapes with large deflections from the spherical geometry. Therefore we can study the effect of tilt order on non-spherical shapes such as the pears and oblates predicted by the fluid membrane model. Rather than studying the transition in the tilt order (as in [59]), we focus on the shape effect: the effect of the tilt modulus K_m (the elastic constant governing the resistance to non-uniform tilt order) on the overall membrane shape.

Topological defects can also form for geometrical reasons, even on surfaces such as tori which do not require any defects in orientational order. Our work is complementary to recent work on the formation and interaction of such defects on a fixed but arbitrarily curved surface [10] [91]. Instead of prescribing the shape and solving for the orientational order field, we prescribe the positions of two defects and solve for the vesicle shape and tilt field. We disallow additional defect formation, and discuss the validity and limitations

of this restriction in Sec. 2.5.

2.3 The Model and Its Analysis

We make several simplifying assumptions in our analysis. Since the vesicles we consider are much larger than their constituent molecules, we use continuum mechanics in the long-wavelength approximation. Thermal fluctuations are disregarded. We assume that the vesicle shapes are surfaces of revolution, and the tilt configuration is axisymmetric. In particular, the defects required by topology are assumed to sit at the two poles of the vesicle. These assumptions reduce the partial differential equations governing the shape and tilt configuration to ordinary differential equations, which greatly simplifies our calculations. Also, we suppose that the bilayer membrane is thin compared to the characteristic size of the vesicle. Since the lipid bilayers are approximately two nanometers thick [63], this assumption is highly accurate for vesicles of micron size and larger. A consequence of this assumption is that stretching is much more costly than bending; therefore, we demand that the total area remain constant. And, although membranes are permeable to water, osmotic effects resist changes in volume [78], leading us to fix the volume. As we explain below, we use a minimal model for the orientational order, disregarding anisotropic couplings between the tilt field and the membrane curvature. We also disregard chiral interactions, which have been shown to be important in models for lipid tubule structure [80] [88] and a proposed mechanism for budding [76, 75].

We will study how vesicle shape depends on area and volume in the presence of tilt order. Just as in the case of fluid membranes, we will see that the bending energy and

tilt stiffness energy terms are scale invariant. This invariance allows us to vary area A and volume V by changing one parameter, the reduced volume v [78]. The reduced volume is the ratio of the actual volume of a vesicle to the volume of a sphere with the same area as the vesicle. If R_0 is the radius of the sphere with area A, then $v = V/(4\pi R_0^3/3)$.

2.3.1 Parametrization and geometry

In this section we describe our parametrization and fix the notation; see [16] and [45] for general discussions of differential geometry applied to membranes. We choose the z axis to be the axis of symmetry of the vesicle and represent points on the surface of the vesicle by the three–dimensional vector $\mathbf{X}(\phi, s) = (r(s)\cos\phi, r(s)\sin\phi, z(s))$, where ϕ and r are plane polar coordinates in the xy plane, and s is the arclength measured from the north pole of the surface along a line of longitude (see Fig. 2.2). Define $\psi(s)$ to be the angle between the tangent vector $\partial_s\mathbf{X}$ along a longitude and the horizontal axis. Then $\mathrm{d}z/\mathrm{d}r = z_s/r_s = -\tan\psi(s)$, where $0 < \psi(s) < \pi$. In terms of ψ, we have $r_s = \cos\psi$ and $z_s = -\sin\psi$.

An orthonormal basis in the tangent plane of the surface is given by

$$\begin{aligned} \hat{\mathbf{e}}_1 &= \partial_s\mathbf{X} = (\cos\psi\cos\phi, \cos\psi\sin\phi, -\sin\psi) \\ \hat{\mathbf{e}}_2 &= \partial_\phi\mathbf{X}/|\partial_\phi\mathbf{X}| = (-\sin\phi, \cos\phi, 0), \end{aligned} \tag{2.1}$$

where the s and ϕ subscripts denote partial differentiation with respect to the coordinates s and ϕ, respectively. We construct the outward normal $\hat{\mathbf{n}}$ to the surface using the

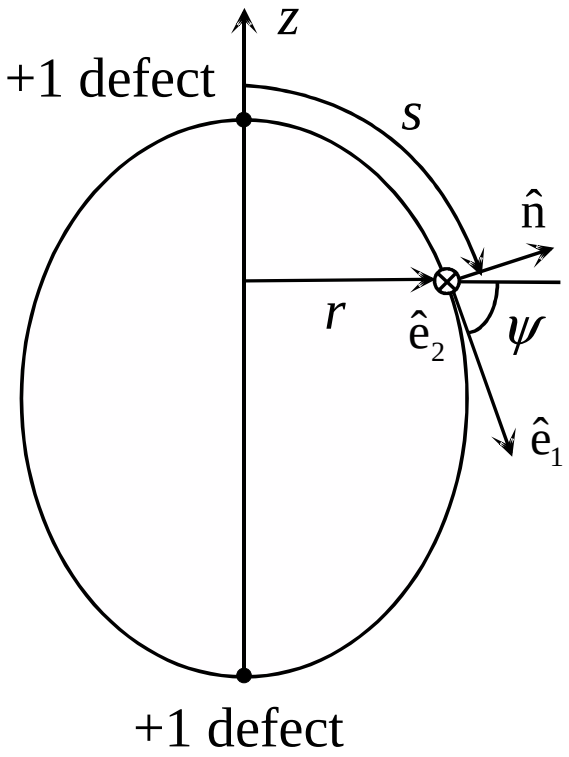

Figure 2.2: Vesicle coordinate system and assumed location of defects. The shape is a surface of revolution about the z axis. The vector $\hat{\mathbf{e}}_2$ points into the page as indicated by the $\otimes$.

orthonormal frame:

$$\hat{\mathbf{n}} = \hat{\mathbf{e}}_1 \times \hat{\mathbf{e}}_2 = (\sin\psi\cos\phi, \sin\psi\sin\phi, \cos\psi). \tag{2.2}$$

The metric tensor g_{ij} of the surface is given by

$$g_{ij} \;=\; \partial_i \mathbf{X} \cdot \partial_j \mathbf{X} = \begin{pmatrix} 1 & 0 \\ 0 & r^2 \end{pmatrix}, \tag{2.3}$$

where the indices $i, j = 1, 2$ label the coordinates s and ϕ, respectively. As usual, we denote the inverse of the metric tensor by g^{ij}, and we use g^{ij} to raise indices. The second

fundamental form K_{ij} is defined by

$$K_{ij} \equiv \hat{\mathbf{n}} \cdot \partial_i \partial_j \mathbf{X} = - \begin{pmatrix} \psi_s & 0 \\ 0 & r \sin \psi \end{pmatrix}. \tag{2.4}$$

From the second fundamental form we construct the mean curvature H and Gaussian curvature K:

$$H \equiv -\frac{1}{2} g^{ij} K_{ij} = \frac{1}{2}(\psi_s + \sin \psi / r) \tag{2.5}$$

$$K \equiv \det(K^i{}_j) = \det(g^{il} K_{lj}) = \psi_s \sin \psi / r, \tag{2.6}$$

where repeated indices have been summed over. Note from Eq. (2.5) that we use a convention in which the sphere has positive mean curvature.

We assume that the lipid molecules on the surface of the vesicle are tilted at a preferred angle with respect to the surface normal $\hat{\mathbf{n}}$, as in a smectic-C phase [17]. Let the vector $\mathbf{m}$ denote the projection of the directors of the lipid molecules onto the tangent plane. Since we do not study the transition between tilted and untilted phases, it is convenient to normalize $\mathbf{m}$ to make $|\mathbf{m}| = 1$ well away from topological defects. In terms of the local orthonormal basis of the tangent plane, we have

$$\mathbf{m} = B(\cos \theta \hat{\mathbf{e}}_1 + \sin \theta \hat{\mathbf{e}}_2) = B \hat{\mathbf{m}}, \tag{2.7}$$

where the amplitude B vanishes at defect centers, and approaches unity far from defect cores.

We must assign an energy penalty to nonuniform configurations of the tilt field $\mathbf{m}$. For a flat surface, $\mathbf{m}$ is uniform if the components of $\mathbf{m}$ are constant in the standard Cartesian basis. Thus, a suitable energy density would be proportional to $\partial_i m^j \partial_i m^j$. However, on a curved surface, $\mathbf{m}$ can vary with position not only because m^i varies with position, but also because $\hat{\mathbf{e}}_i$ can vary. Furthermore, it is only the tangential component of derivatives of $\mathbf{m}$ that enter the tilt stiffness terms; normal components add to the resistance to bending and therefore may be absorbed in the bending energy term, discussed below. These features are captured by the covariant derivative

$$\begin{aligned} D_i\mathbf{m} &= \partial_i\mathbf{m} - (\hat{\mathbf{n}}\cdot\partial_i\mathbf{m})\hat{\mathbf{n}} \\ &= (\partial_i m^1 - m^2\Omega_i)\hat{\mathbf{e}}_1 + (\partial_i m^2 + m^1\Omega_i)\hat{\mathbf{e}}_2, \end{aligned} \tag{2.8}$$

where the "spin connection,"

$$\Omega_i = \hat{\mathbf{e}}_2 \cdot \partial_i \hat{\mathbf{e}}_1, \tag{2.9}$$

is the rate at which the frame $\{\hat{\mathbf{e}}_1, \hat{\mathbf{e}}_2\}$ rotates about the normal $\hat{\mathbf{n}}$ as the ith coordinate increases. The covariant curl of the spin connection is the Gaussian curvature:

$$K = -\frac{1}{\sqrt{g}}\epsilon_{ij}\partial_i\Omega_j, \tag{2.10}$$

where g is the determinant of the metric tensor and ϵ_{ij} is the antisymmetric symbol with $\epsilon_{12} = 1$ [45]. We can now see why Gaussian curvature is incompatible with a uniform tilt field. Consider a tilt field on a surface of nonzero Gaussian curvature. A tilt field on a curved surface is uniform if it has a vanishing covariant derivative. Writing Eq. (2.8) in

terms of B and θ, we find that $D_i\mathbf{m} = 0$ implies $\partial_i B = 0$ and $\partial_i\theta + \Omega_i = 0$. Consider a patch on a curved surface that includes no defects, so that θ is smooth. Then to solve $\partial_i\theta + \Omega_i = 0$ for θ we must have $\epsilon_{ij}\partial_i\Omega_j = 0$ [45]. Therefore, the tilt field cannot be uniform on a patch with Gaussian curvature.

For our parametrization, $\Omega_i = (0, \cos\psi)$: the frame $\{\hat{\mathbf{e}}_1, \hat{\mathbf{e}}_2\}$ rotates about the normal as ϕ changes, but not as s changes. Consistent with our assumption that the shape of the surface is axisymmetric, we assume that the orientation of the molecules is axisymmetric as well, with $\partial_\phi B = 0$ and $\partial_\phi\theta = 0$. Therefore,

$$D_\phi\mathbf{m} = B\cos\psi\hat{\mathbf{m}}_\perp \tag{2.11}$$

$$D_s\mathbf{m} = B_s\hat{\mathbf{m}} + B\theta_s\hat{\mathbf{m}}_\perp, \tag{2.12}$$

where $\hat{\mathbf{m}}_\perp = -\sin\theta\hat{\mathbf{e}}_1 + \cos\theta\hat{\mathbf{e}}_2$, $B_s = \partial_s B$, and $\theta_s = \partial_s\theta$.

2.3.2 Free energy

The free energy F of the vesicle is the sum of terms associated with the bending of the vesicle and terms associated with the tilt vector order parameter field: $F = F_b + F_m$. We use the Helfrich model for bending energy,

$$F_b = \int \left[\frac{\kappa}{2}(2H - c_0)^2 + \kappa_G K\right]\sqrt{g}\,\mathrm{d}s\mathrm{d}\phi, \tag{2.13}$$

In Eq. (2.13), κ is the bending modulus, typically 10–15$k_\mathrm{B}T$ [63], and κ_G is the Gaussian rigidity. The spontaneous curvature c_0 is twice the preferred value of the mean curvature for a patch of membrane. Spontaneous curvature of a bilayer membrane can arise either

from the sum of the inherent spontaneous curvatures of the monolayers, or from a difference in the number of molecules in either monolayer [20]. Since we consider a closed surface with fixed topology, the Gauss-Bonnet theorem ensures that the integral of the Gaussian curvature is independent of shape and contributes only an overall constant to the free energy [62]. Therefore the term proportional to κ_G may safely be disregarded.

The elastic free energy F_m for the tilt order is a sum of many terms, including costs for splay and bend of the director field, and many terms coupling the director field to the vesicle shape [65, 69]. To simplify our task, we demand that the energy be isotropic in tilt, i.e. invariant under arbitrary rotations of $\mathbf{m}$ about the normal $\hat{\mathbf{n}}$. This symmetry rules out all of the anisotropic terms, leaving only a minimal coupling of the tilt order to shape:

$$\begin{aligned} F_m &= \frac{1}{2}\int \Big[K_m D_i m^j D^i m_j \\ &\quad + \frac{\lambda}{2}(1 - m_i m^i)^2\Big]\sqrt{g}\,\mathrm{d}s\mathrm{d}\phi. \end{aligned} \tag{2.14}$$

The first term of Eq. (2.14) gives a preference for a uniform tilt field. Since we impose isotropy, the free energy density at a point is independent of the direction of $\mathbf{m}$ relative to the principal directions of curvature. (We discuss how anisotropy may affect our results in Sec 2.5). Note that the Frank elastic constant K_m has the same dimensions as κ, implying that the effects of this term are comparable to the effects of the bending term of Eq. (2.13). We know of no measurements of K_m in vesicles, but by dimensional analysis we expect that K_m is comparable to κ. This argument gives good estimates for the Frank constants in three-dimensional liquid crystal systems [17]. In the absence of concrete measurements, our calculations will explore a reasonable range of K_m/κ. The second term of Eq. (2.14)

gives a preference for $|\mathbf{m}| = 1$. We assume that we are deep in the ordered phase, so that $\lambda R_0^2/K_m \gg 1$. The length scale $\sqrt{K_m/\lambda}$ determines the radius of the defect core, wherein $|\mathbf{m}|$ falls steeply to zero.

The shape of the vesicle and the orientation of the tilted molecules on its surface are determined by minimizing F subject to a given surface area A and volume V. To impose these constraints, we introduce Lagrange multipliers Σ and P. It is convenient to treat r and ψ as independent variables in the variation of the free energy. Therefore, we introduce an additional Lagrange multiplier function $\gamma(s)$ to impose the local constraint $r_s = \cos\psi$. Thus, our task is to minimize

$$F' \equiv F + \Sigma A + PV + \kappa \int \gamma(s)(r_s - \cos\psi)\mathrm{d}s\mathrm{d}\phi. \tag{2.15}$$

It is convenient to scale the Lagrange multipliers by κ: $\bar{\Sigma} = \Sigma/\kappa$ and $\bar{P} = P/\kappa$. Then F' can be written as

$$F' \;=\; 2\pi\kappa \int_0^L f'(\psi, \psi_s, r, r_s, B, B_s, \theta_s, \gamma)\,\mathrm{d}s, \tag{2.16}$$

where the upper integration limit L is the total arclength along a longitude from the north

to the south pole, and

$$
\begin{aligned}
&f'(\psi, \psi_s, r, r_s, B, B_s, \theta_s, \gamma) \\
&= r\left[\frac{1}{2}(\sin\psi/r + \psi_s - c_0)^2 + \bar{\Sigma} + \frac{1}{2}\bar{P}r\sin\psi\right. \\
&\left.+\frac{\lambda}{4\kappa}(1-B^2)^2 + \frac{K_m}{2\kappa}(B^2\cos^2\psi/r^2 + {B_s}^2 + B^2\theta_s^2)\right] \\
&+\gamma(s)(r_s - \cos\psi). \qquad (2.17)
\end{aligned}
$$

2.3.3 Euler-Lagrange equations

The Euler-Lagrange equations which extremize F' are given by

$$
\begin{aligned}
\psi_s &= \frac{U}{r} - \frac{\sin\psi}{r} + c_0, && (2.18)\\
U_s &= \frac{U}{r}\cos\psi + \gamma\sin\psi + \frac{1}{2}\bar{P}r^2\cos\psi \\
&\quad -\frac{K_m B^2}{\kappa r}\cos\psi\sin\psi, && (2.19)\\
B_s &= \frac{\kappa W}{K_m r}, && (2.20)\\
W_s &= -\frac{\lambda}{\kappa}rB(1-B^2) \\
&\quad +\frac{K_m r B}{\kappa}\left(\frac{\cos^2\psi}{r^2} + \theta_s^2\right), && (2.21)\\
\gamma_s &= \frac{U^2}{2r^2} - \frac{U}{r^2}\sin\psi + \bar{P}r\sin\psi + \bar{\Sigma} \\
&\quad +\frac{K_m}{2\kappa}\left[-\frac{B^2}{r^2}\cos^2\psi + \left(\frac{\kappa W}{K_m r} + B^2\theta_s^2\right)^2\right] \\
&\quad +\frac{\lambda}{4\kappa}(1-B^2)^2, && (2.22)\\
r_s &= \cos\psi, && (2.23)\\
\left(rB^2\theta_s\right)_s &= 0. && (2.24)
\end{aligned}
$$

We have introduced two auxiliary functions U and W to obtain first-order differential equations, which are required for our numerical routine.

The Euler-Lagrange equations can be simplified somewhat by the observation that θ is independent of s. Equation (2.24) implies that $rB^2\theta_s$ is independent of s. However, because r and B both vanish at the poles, $rK'_mB^2\theta_s = 0$ everywhere. Since B and r are nonzero only right at the poles, $\theta_s = 0$ everywhere. This result can be seen more directly by examining the form of the free energy F_m, Eq. (2.14). Since $\Omega_s = \Omega_1 = 0$, F_m is minimized when θ is independent of s. Note that the isotropy of the energy means that F is independent of the angle θ. In Fig. 2.1, for example, we chose to have the directors aligned with lines of latitude. The choice was arbitrary – directors aligned along lines of longitude, or any other direction, would result in the same free energy and same shape.

For the remaining six equations (2.18–2.23) we have six corresponding boundary conditions. The angle ψ and radius r are fixed at either pole: $\psi(0) = r(0) = r(L) = 0$, and $\psi(L) = \pi$. The amplitude B at either pole vanishes due to the assumed presence of defects, $B(0) = B(L) = 0$. However, L is still unknown and must be solved for along with the shape. To determine L, we reparametrize the problem, introducing a new independent variable t such that $t = 0$ at the north pole and $t = 1$ at the south pole: $s = Lt$, where L is a constant [43]. The Euler-Lagrange equations (2.18–2.24) are therefore modified by replacing $\mathrm{d}/\mathrm{d}s$ with $(1/L)\mathrm{d}/\mathrm{d}t$. Note that the boundary conditions on r, ψ, and B at $s = L$ become boundary conditions at $t = 1$. The additional equation allowing us to solve for L is $\mathrm{d}L/\mathrm{d}t = 0$. To determine the additional boundary condition required by this equation, we consider the symmetry of the free energy under a constant shift in s. The free energy

density now takes the form $F' = 2\pi\kappa \int_0^1 \tilde{f} \mathrm{d}t$, where

$$\begin{aligned} &\tilde{f}(\psi, \psi_t, r, r_t, B, B_t, \theta_t, \gamma, s_t) \\ &= s_t f'(\psi, \psi_s/L, r, r_s/s_t, B, B_s/s_t, \theta_s/s_t, \gamma), \end{aligned} \tag{2.25}$$

and $s_t = L$. Since $s(t)$ does not appear explicitly in the free energy density, there is a first integral or Hamiltonian function $\partial\tilde{f}/\partial s_t$ which is independent of t. Examination of the variation of $\tilde{f}$ with respect to $s(t)$ leads to $\partial\tilde{f}/\partial s_t = 0$ at $t = 1$, implying that the Hamiltonian function vanishes everywhere. Writing the Hamiltonian explicitly in terms of the dependent variables at $t = 0$ yields the desired boundary condition $\gamma(0) = 0$ [79, 43].

To complete our specification of the shape equations, we describe how we implement the constraints of fixed area and volume. It is convenient to regard area as a function of t. Define $A(t)$ as the area of the portion of the vesicle surface north of the line of latitude corresponding to t, with a similar definition for $V(t)$. Then

$$A_t = 2\pi r L \tag{2.26}$$

$$V_t = \pi r^2 \sin\psi L \tag{2.27}$$

$$\bar{\Sigma}_t = 0 \tag{2.28}$$

$$\bar{P}_t = 0, \tag{2.29}$$

where Eqs. (2.28)–(2.29) arise because the Lagrange multipliers are constant, but unknown and shape-dependent. The four boundary conditions corresponding to Eqs. (2.26–2.29) are $A(0) = 0$, $A(1) = 4\pi R_0^2$, $V(0) = 0$, and $V(1) = 4\pi R_0^3 v/3$. The scale R_0 is set to unity in

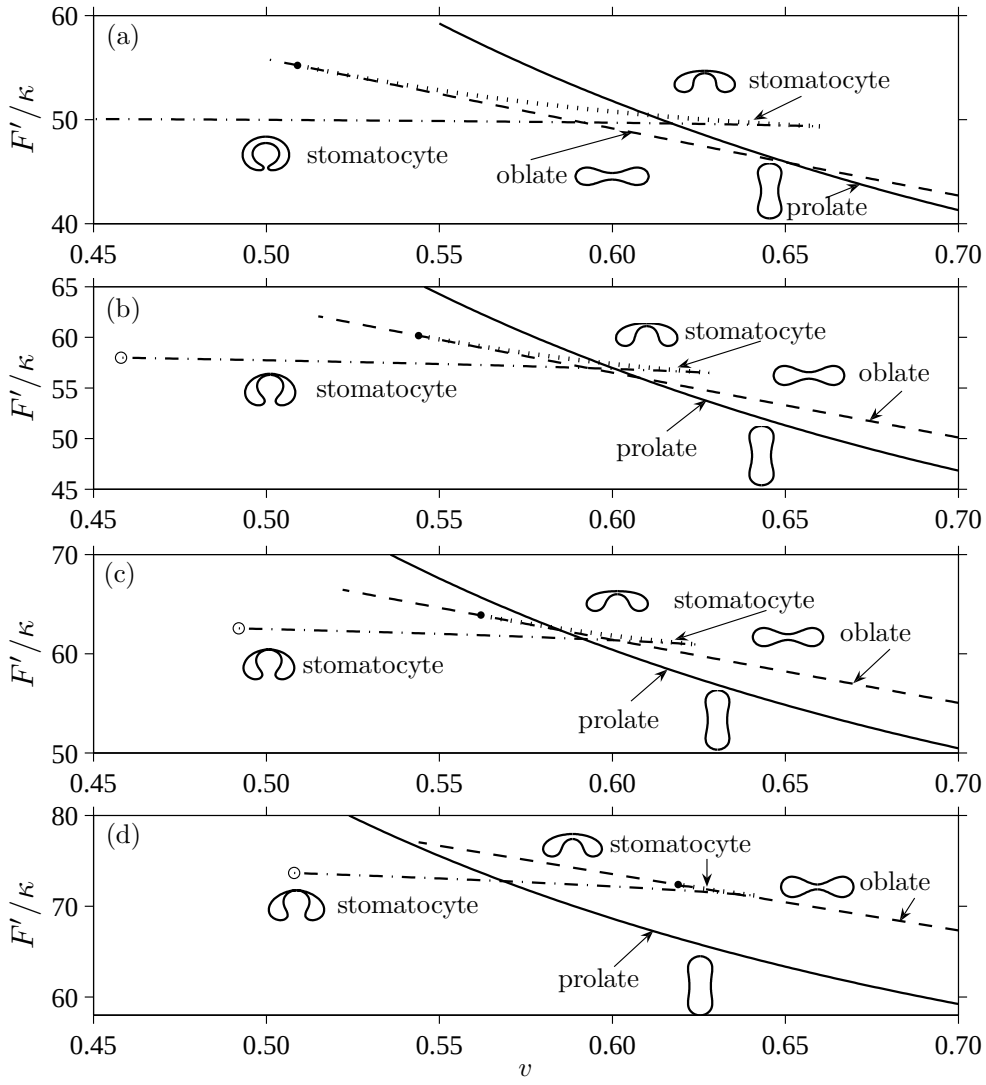

Figure 2.3: Dimensionless free energy F'/κ vs. reduced volume v for fluid membrane vesicles with $c_0 = 0$ for three different values of Frank elastic constant: (a) $K_m = 0$. (b) $K_m = 0.3\kappa$. (c) $K_m = 0.5\kappa$ (d) $K_m = \kappa$. Solid lines correspond to prolate shapes, dashed lines correspond to oblate shapes, and the dash-dotted and dotted lines correspond to stomatocyte shapes. The filled circles denote continuous bifurcations. The open circles denote limit points at which the vesicle intersects itself.

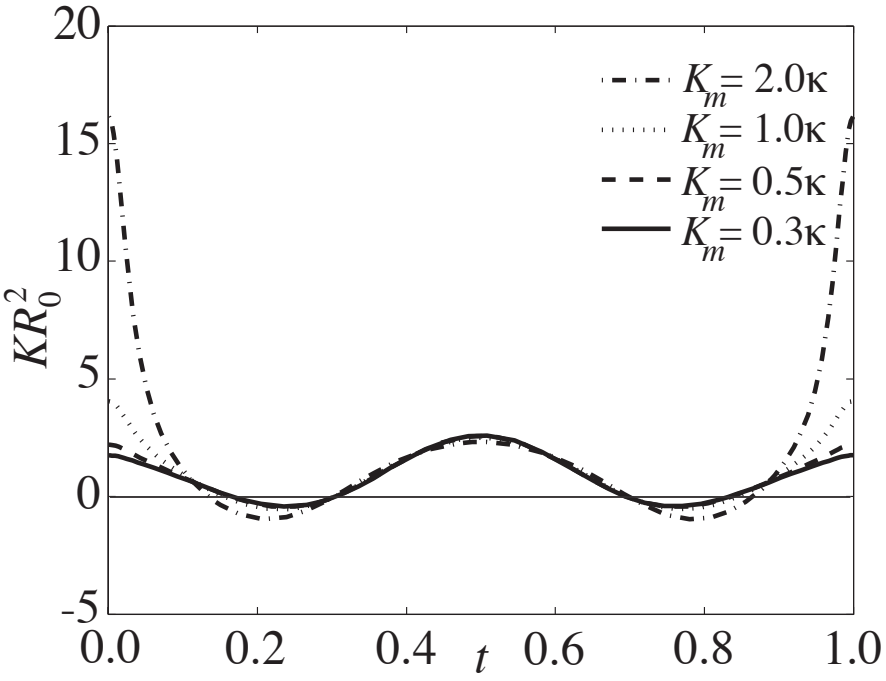

Figure 2.4: Dimensionless Gaussian curvature KR_0^2 versus the dimensionless parameter t for oblate shapes with $c_0 = 0$ and various values of K_m/κ. Note that $t = 0$ at the north pole, $t = 1$ at the south pole, and $t = 0.5$ at the equator, which lies in the horizontal plane midway between the two defects.

our numerical calculations. Finally, the shape is determined by integrating $z_t = -L \sin\psi$ with boundary condition $z(0) = 0$.

Although the Euler-Lagrange equations are nonlinear and must be solved numerically, it is straightforward to determine the form of the amplitude B at the centers of the defect cores. For example, near $s = 0$, we have $\cos\psi \approx 0$ and $r \approx s$. Therefore, equations (2.20) and (2.21) reduce to Bessel's equation for $s \approx 0$:

$$s^2 B_{ss} + s B_s + \left(\frac{\lambda}{K_m} s^2 - 1 \right) B = 0, \tag{2.30}$$

and thus $B \propto s$ in the core, which has a size set by $\sqrt{K_m/\lambda}$, as mentioned earlier. Similar

considerations apply to the defect located at the south pole.

In our numerical approach, we treat the Euler–Lagrange equations as a two-point boundary value problem, using the MATLAB function `bvp4c` [81]. We choose $\lambda/K_m = 1000$ to make the defect cores small. To avoid the divergences that occur in the equations when $r \to 0$, we solve the equations in the interval $\delta < t < 1-\delta$, where $\delta = 0.001$. All boundary conditions are now evaluated at $t = \delta$ or $t = 1-\delta$. We use Taylor series to relate the boundary values at these new endpoints to the values at $t = 0$ and $t = 1$:

$$\psi(\delta) \approx \psi(0) + \psi_t(0)\delta = \psi_t(0)\delta \tag{2.31}$$

$$B(\delta) \approx B(0) + B_t(0)\delta = B_t(0)\delta \tag{2.32}$$

$$\psi(1-\delta) \approx \psi(1) - \psi_t(1)\delta = \pi - \psi_t(1)\delta \tag{2.33}$$

$$B(1-\delta) \approx B(1) - B_t(1)\delta = -B_t(1)\delta. \tag{2.34}$$

The constants $\psi_t(0)$, $B_t(0)$, $\psi_t(1)$, and $B_t(1)$ are unknown parameters that may be determined by the numerical routine using the conditions

$$U(\delta) \approx L\psi_t(\delta)r(\delta) + \sin(\psi(\delta)) + c_0 r(\delta) \tag{2.35}$$

$$\begin{aligned} U(1-\delta) &\approx L\psi_t(1-\delta)r(1-\delta) \\ &+ \sin(\psi(1-\delta)) + c_0 r(1-\delta) \end{aligned} \tag{2.36}$$

$$W(\delta) \approx LB_t(\delta)K_m r(\delta)/\kappa \tag{2.37}$$

$$W(1-\delta) \approx LB_t(1-\delta)K_m r(1-\delta)/\kappa. \tag{2.38}$$

from Eqns. (2.18) and (2.20). We also have

$$\begin{aligned} \gamma(\delta) &= \gamma(0) + \gamma_t(0)\delta \\ &\approx \gamma(0) + \gamma_t(\delta)\delta = \gamma_t(\delta)\delta, \end{aligned} \tag{2.39}$$

with an error of order δ^2. The parameter $\gamma_t(\delta)$ is given in terms of the variables at $t = \delta$ by Eqn. (2.22).

2.4 Results

For purposes of comparison with the case of a fluid membrane with no tilt order, we have repeated the calculations of Ref. [79] for spontaneous curvature $c_0 = 0$ and $c_0 R_0 = 2.4$. At $v = 1$, the vesicle shape is always spherical, with bending energy $8\pi\kappa$. First consider the case $c_0 = 0$. As v is decreased from unity, the lowest energy shape becomes prolate, elongating continuously. Upon further decrease of v the shape changes discontinuously to oblate, and finally to the stomatocyte shape. At $v = 0$ where the dash-dotted line in Figure 2.3a terminates, the stomatocyte shape consists of two concentric spheres, spaced infinitesimally close, connected by a vanishingly thin neck of zero mean curvature, with a total bending energy $16\pi\kappa$. Figure 2.3a shows some of these shapes, and the free energy vs. v over the range for which the transitions occur. Note that there are two stomatocyte branches; the upper one (dotted line) is metastable. As the reduced volume is decreased along the upper stomatocyte branch, the vesicle height along the z axis decreases and the shape becomes more symmetric about the horizontal plane midway between the two defects. The two branches join at the filled circle, where the stomatocyte shape becomes

oblate. Figures 2.3b and c show the effect of tilt order. As K_m/κ increases, the prolate branch of solutions has lower free energy than the oblate branch for a greater range of reduced volume, until eventually the oblate branch becomes completely metastable. To understand why tilt order favors prolate shapes over oblate, note that as v decreases, the prolate shapes extend more along the z axis and become more cylindrical, leading to a greater region of small Gaussian curvature and approximately uniform tilt order. The oblate shapes also have regions of small Gaussian curvature, but these regions are confined to narrow bands near $t \approx 0.2$ and $t \approx 0.8$ (Fig. 2.4).

Figure 2.4 also shows that our assumption that the defects are constrained to lie at the poles of the vesicle is reasonable. Defects of positive sign prefer regions of positive Gaussian curvature [11]. Figure 2.4 shows that for $K_m/\kappa \lesssim 0.5$, the Gaussian curvature at the equator is just greater than the Gaussian curvature at either pole. Thus, for $K_m \lesssim 0.5\kappa$, we expect that the configuration with two defects at antipodal points on the equator might have smaller energy than the configuration with defects on either pole. Our simplifying assumption of axisymmetry prevents us from investigating this possibility. However, as K_m/κ is increased to unity, the regions of maximum Gaussian curvature lie at the poles, and we expect that the minimum energy configuration is to have the defects lie at the poles. For the prolate shapes and the pear shapes considered below, the poles are always regions of maximum Gaussian curvature. Even for the stomatocyte, the north pole is the region of maximum Gaussian curvature, and the Gaussian curvature is roughly constant over much of the inner surface of the pocket.

A second qualitative effect of tilt order on the $c_0 = 0$ shapes is that the lower stomatocyte branch develops a limit point corresponding to self-intersection at the sites of the

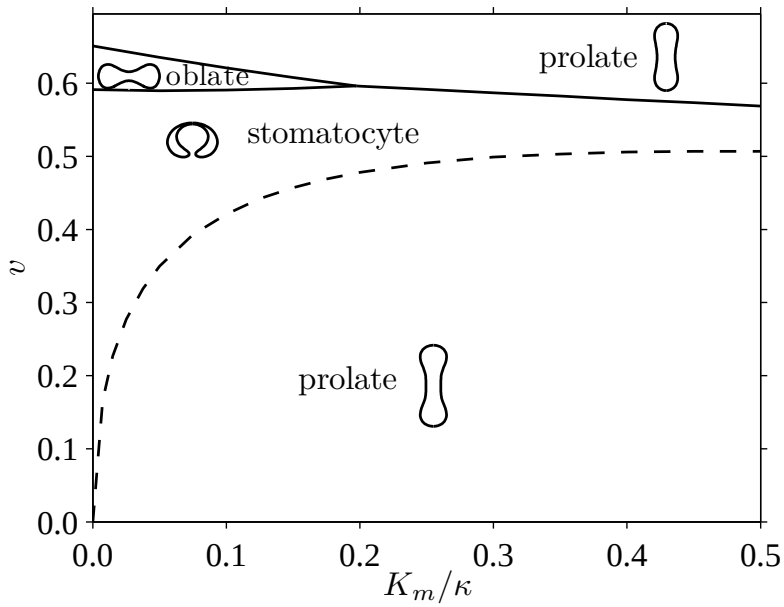

Figure 2.5: Phase diagram for lowest energy vesicle shapes for $c_0 = 0$. The lowest energy shapes are shown for each value of v and K_m/κ. The dashed line denotes the line of limit points for the stomatocyte shapes.

defects. These limit points are denoted by open circles in Fig. 2.3b and c. Figure 2.5 shows the phase diagram for the lowest energy vesicle shapes for the case $c_0 = 0$ as a function of the Frank constant. The dashed line shows the values of K_m/κ and v for which the stomatocyte shape intersects itself. For values of v below the dashed line, the prolate branch again becomes the lowest energy branch of solutions.

Turning to the case $c_0R_0 = 2.4$, we see from Ref. [79] that the fluid membrane shapes are dominated by prolate shapes and pear shapes, Fig. 2.6a. Note that the energy scale on the vertical axis is much less than that of Fig. 2.3a since the mean curvature required by the constraints of fixed volume and area is close to c_0. The solid dots again denote continuous transitions between pear and prolate shapes. The effect of tilt order is to increase the energy cost of the pear shapes relative to the prolate shapes, eventually making the prolate

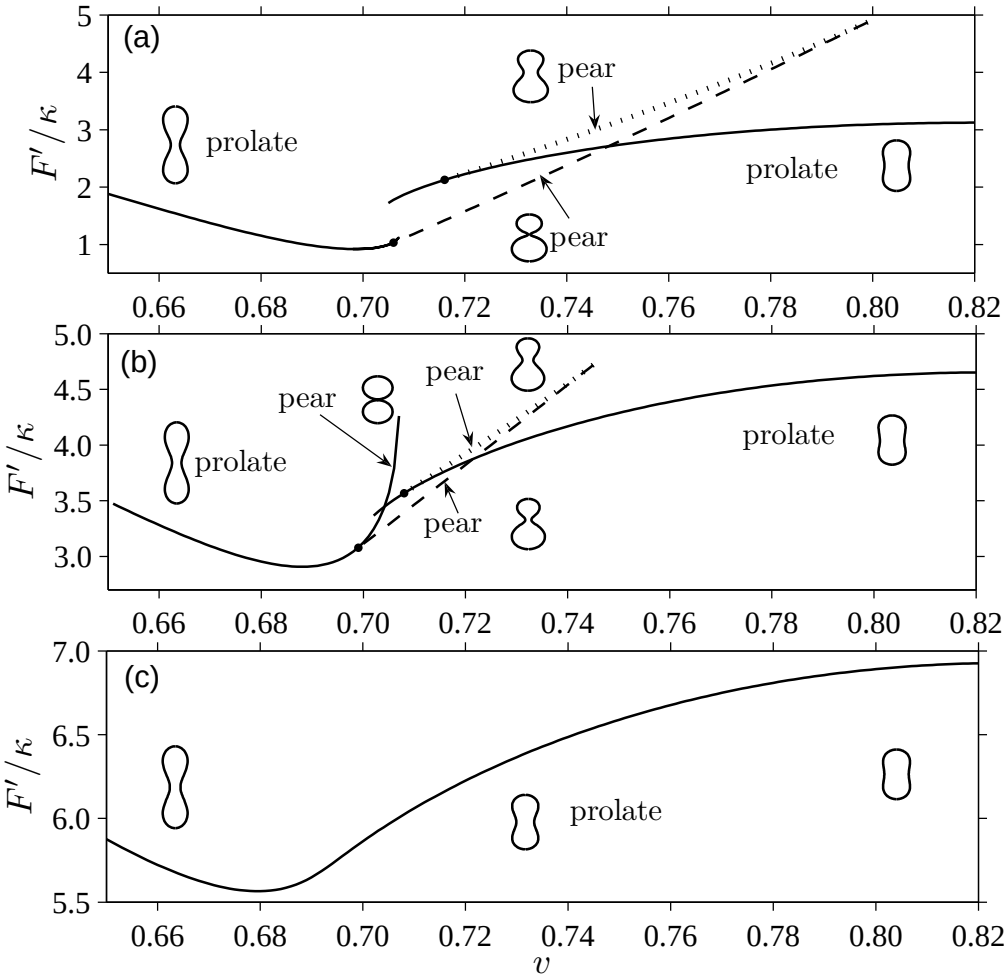

Figure 2.6: Dimensionless free energy F'/κ vs. reduced volume v for fluid membrane vesicles with $c_0R_0 = 2.4$ and three different values of Frank elastic constant: (a) $K_m/\kappa = 0$, (b) $K_m/\kappa = 0.08$, (c) $K_m/\kappa = 2.0$. Solid lines correspond to prolate shapes, dashed lines correspond to asymmetric pear shapes, and the dotted line corresponds to symmetric pear shapes. The filled circles mark continuous bifurcations. There is a symmetric pear branch in (a), just to the right of the first bifurcation, but it is too short to be seen.

branch of solutions the lowest energy branch for all v. It is interesting to note that tilt order does not completely rule out pear shapes with narrow necks. The phase diagram of lowest energy shapes in Fig. 2.7 shows that pear shapes are allowed in a range of v for sufficiently small K_m. The neck of the pear shape becomes wider as K_m increases. For these shapes, there is a slight reduction in the order B in a narrow band around the neck.

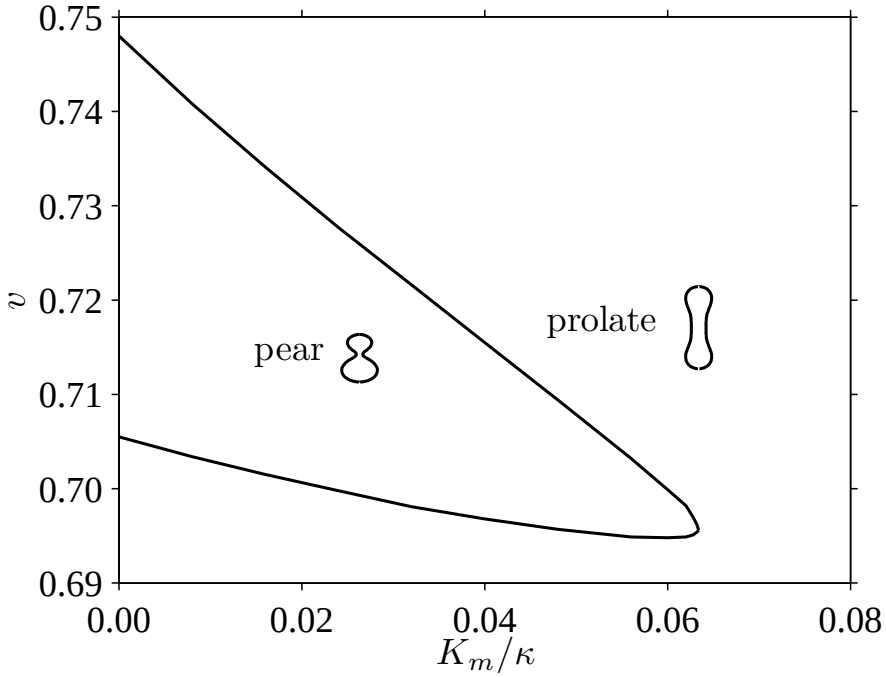

Figure 2.7: Phase diagram for $c_0R_0 = 2.4$. The lowest energy shapes are shown for each value of v and K_m/κ.

2.5 Discussion and conclusion

Our detailed, systematic calculations show that tilt order suppresses necks and favors elongated prolate shapes for sufficiently large tilt modulus K_m. We calculated the free energy as a function of reduced volume for several branches of solutions, and showed how

increasing the tilt modulus increases the energy of the non-prolate branches relative to the prolate branches, finally leading to a single family of prolate shapes.

Our calculation was based on several important assumptions. We ruled out many of the possible terms in the free energy by taking the free energy to be invariant under arbitrary rotations of $\hat{\mathbf{m}}$ about the normal $\hat{\mathbf{n}}$. A natural way to remove this assumption and study the effects of anisotropy without introducing an unmanageable number of terms would be to replace F_m with F_d, the one-Frank-constant approximation for the orientational free energy of the directors $\hat{\mathbf{d}}$ making up the membrane surface [80]:

$$F_d = \frac{K_m}{2} \int \left(\partial_i \hat{\mathbf{d}} \cdot \partial_j \hat{\mathbf{d}} \right) g^{ij} \sqrt{g} \mathrm{d}s\mathrm{d}\phi. \tag{2.40}$$

To compare F_d with F_m, write $\hat{\mathbf{d}} = \alpha \hat{\mathbf{N}} + \mathbf{m}$, where $\hat{\mathbf{N}}$ is the local unit surface normal, and α is determined by $|\hat{\mathbf{d}}| = 1$. Rewriting F_d in terms of intrinsically two-dimensional quantities, we find that

$$\begin{aligned} F_d &= \frac{K_m}{2} \int \Big[g^{ij} \nabla_i m^k \nabla_j m_k + \alpha^2 K_i^j K_j^i \\ &+ m^i K_{ij} K_k^j m^k - 2\alpha \left(\nabla_i m^j \right) K_j^i \Big] \sqrt{g} \mathrm{d}s\mathrm{d}\phi. \end{aligned} \tag{2.41}$$

The first two terms of the integrand in (2.41) are isotropic. To see that the term $K_i^j K_j^i$ is already accounted for in our minimal isotropic tilt model, note that a matrix satisfies its own characteristic equation:

$$K_k^i K_j^k - K_j^i K_k^k + K \delta_j^i = 0. \tag{2.42}$$

Using g^{ij} to take the trace of Eq. (2.42) yields $K^i_j K^j_i = 4H^2 - 2K$. We expect that the term $m^i K_{ij} K^j_k m^k$ leads to a preference for the tilt to order along the long axis of a prolate shape, and an increased bending stiffness along the direction parallel to $\hat{\mathbf{m}}$. The last term in the integrand of (2.41) is like a spontaneous curvature given by a gradient of the projected director. Except for the fact that the anisotropic terms will lead to a preferred direction of $\hat{\mathbf{m}}$ relative to the principal directions of curvature, we expect that including these terms would not qualitatively change our results. A more dramatic change is expected if chiral terms like $m^i \epsilon_{ij} K^j_k m^k$ are allowed. This term can give the vesicle a chiral shape, which is necessarily non-axisymmetric. It would be interesting to add this term alone to our minimal model and study vesicles shapes, as has recently been done for tubules and ribbons [88].

The most severe assumption of our model is the assumption of fixed defects at the poles. We have already mentioned that positive sign defects prefer regions of positive curvature, which suggests there may be lower energy, non-axisymmetric shapes than the ones we consider here. Furthermore, recent calculations have shown how a pair of defects of opposite sign can be pulled apart whenever there is a change in sign in the Gaussian curvature, with the positive defect migrating to the region of positive Gaussian curvature, and the negative defect migrating to the region of negative Gaussian curvature [91]. The magnitude of the curvature in both regions is important for determining whether or not a defect pair will unbind. Although we completely disregard this effect, we expect it will not play much of a role in the low-energy prolate shapes, since for those shapes there are at most only narrow bands of mildly negative Gaussian curvature where either end starts to bow out. An important extension of our calculation would be to lift the assumption of

axisymmetry, and allow both the defect position and number and vesicle shape to vary. It would be interesting if the techniques of Ref. [94] could be used to experimentally determine defect position on vesicles with tilt order.

Finally, we have systematically studied the effect of changing the tilt modulus K_m while deep in the ordered phase. While we have not presented results on the change in shape due to a phase transition from an ordered tilt phase to a disordered fluid phase, as in Ref. [59], we expect that the effect of increasing the order should be qualitatively similar to increasing K_m.

Chapter 3

Lipid rafts in multi-component membranes

3.1 Curvature-driven lipid sorting in a membrane tubule

3.1.1 Introduction

Since lipid molecules have both hydrophobic and hydrophilic properties, they naturally self-assemble into membranes that form sealed containers. But in the living cell, these structures are neither static nor passive. For example, the membranous organelles of eukaryotic cells exchange material through a continual traffic of membrane vesicles. Although this process is highly regulated by proteins, generic physical properties of lipid molecules are crucial for steps in membrane trafficking such as budding, fission, and fusion [61]. Since material is constantly exchanged, lipids and proteins must be sorted to maintain the distinct compositions of organelles [64]. Recent in vitro experiments with lipid mixtures with

well-characterized phase behavior have shown that membrane curvature can determine how lipid mixtures segregate [2, 72]. Cell motility offers a second example of membrane curvature coupling to molecular organization, since the composition of the plasma membrane in the highly curved tips of filopodia differs from that of flat regions [3].

Many previous theoretical studies have considered the coupling of membrane composition and bending arising from the shape of protein or lipid molecules diffusing in one of the leaflets of the bilayer [51]. Here we consider a different mechanism for coupling membrane composition and membrane bending. Mixtures of lipids can separate into different coexisting phases. For example, ternary mixtures of dioleoylphosphatidylcholine (DOPC), sphingomyelin (SM), and cholesterol can form liquid-disordered (L_d) and liquid-ordered (L_o) phases [89]. The chains of the lipids are ordered in the L_o phase but not in the L_d phase. The ordered chains of the L_o phase make the membrane thicker and therefore stiffer compared to a membrane in the L_d phase. Thus, it is natural to expect that the L_d domains will be found in regions of high curvature when the two phases coexist in a single membrane, as has been found in tubules drawn from multicomponent vesicles [2] and bilayers supported on substrates with varying curvature [72].

Membrane tubules with a typical diameter of tens of nanometers provide an ideal situation for studying this mechanism for coupling curvature and composition, since both degrees are freedom may vary but the geometry is simple. Also, membrane tubules are ubiquitous structures that arise in membrane trafficking [23, 61] as well as artificial situations such as assays for measuring membrane stiffness [33]. In this letter, we develop a simple theory to model the phase-dependence of the membrane bending stiffness and apply it to membrane tubules. We quantitatively show how the high curvature of a membrane

tubule can lead to sorting of lipids and proteins. The simple geometry of the tubule illustrates the more general phenomenon of how membrane curvature can localize particular molecules to specific regions. We show that the force required to form a membrane tubule is reduced by lipid sorting, and also how the coupling of curvature and composition can lead to a discontinuous force-extension relation for a tubule.

Our work is complementary to studies of vesicles with coexisting phases [7], in which bending and line tension effects balance to determine shape [55, 77, 43]. We use a simple model geometry in which a point force pulls a tubule from a disk of membrane attached to a circular ring of radius R_0 [70, 37]. Our work is related to other studies of coexisting phases on membrane tubules [39, 38], but our theory emphasizes the phase transition driven by the difference in bending stiffness mentioned above.

3.1.2 The model

To focus on the essential physical elements of the problem, we replace the ternary lipid mixture with a model in which there is a single type of lipid that can exist in two states, A and B. In state A, the lipid molecule has disordered chains, leading to a relatively large lateral area per molecule and relatively small membrane thickness. In state B, the lipid molecule has ordered chains, with smaller lateral area per molecule and larger membrane thickness. The molecules are free to diffuse, and when there is coexistence the molecules phase separate into an A-rich phase 1, corresponding to $\mathrm{L_d}$, and a B-rich phase 2, corresponding to $\mathrm{L_o}$. The domain structure is modeled using the free energy [51]

$$F_1 = \int \left[\frac{\lambda}{2}\phi^2(1-\phi)^2 + \frac{\mu}{2} g^{ij} \frac{\partial \phi}{\partial u_i} \frac{\partial \phi}{\partial u_j} \right] \sqrt{g}\, \mathrm{d}^2 u, \tag{3.1}$$

where $\phi = (c_{\mathrm{A}} - c_1)/(c_2 - c_1)$; c_{A} is the concentration of A; c_1 and c_2 are the concentrations of A in phase 1 and phase 2, respectively, on a flat membrane; λ and μ are positive material constants arising from intermolecular interactions; u_1 and u_2 are coordinates for the membrane surface; g^{ij} is the contravariant metric tensor; and g is the determinant of the metric tensor. The width of a domain boundary is set by the length $\sqrt{\mu/\lambda}$. There is no physical reason for the free energy to be even in ϕ, but we enforce this symmetry to simplify the analysis. Note that even without this simplification, the number of A molecules is not conserved since the A's and B's can interconvert. A more realistic binary mixture model would have separate conservation of A's and B's in a complete vesicle, with conservation enforced by Lagrange multipliers. These new terms will affect the quantitative details of our results but not the essential nature of our predictions.

Shape changes of the membrane are governed by the Canham-Helfrich energy [13, 34] modified to account for coupling between the composition and the shape,

$$F_2 = \int \left[\frac{\kappa(\phi)}{2} (2H)^2 + \sigma(\phi) \right] \sqrt{g}\, \mathrm{d}^2 u, \tag{3.2}$$

where H is the mean curvature. There is no spontaneous curvature in our model. The bending stiffness $\kappa(\phi)$ depends on composition since membrane in phase 1 is thinner and therefore more flexible than membrane in phase 2. We use $\kappa(\phi) = \kappa_0[1 + \alpha_1(\phi^2 - 1)]$ with $\alpha_1 > 0$; experiments indicate that a reasonable value for α_1 is ≈ 0.5 [7, 2]. Since the chains of a B molecule take up less lateral area than the chains of an A, we expect that imposed tension can cause a transition from B to A. Thus we take $\sigma(\phi) = \sigma_0[1 + \alpha_2(\phi^2 - 1)]$ with $\alpha_2 > 0$. The coupling constant α_2 favors phase 1 in the presence of tension σ_0. Both $\kappa(\phi)$

and $\sigma(\phi)$ are chosen to be even in ϕ for the convenience of maintaining the equilibrium value of $\phi = 0$ in the A-rich phase; the coupling of composition with curvature and tension shifts the equilibrium value of ϕ in the B-rich phase slightly away from unity.

To keep the model simple, we have not included Gaussian curvature terms in Eq. (3.2); the effect of the disregarded terms is to shift the position of a domain boundary [42]. Coupling of Gaussian curvature and composition can also lead to thin necks which could promote fission [12, 39], an effect beyond the scope of our work.

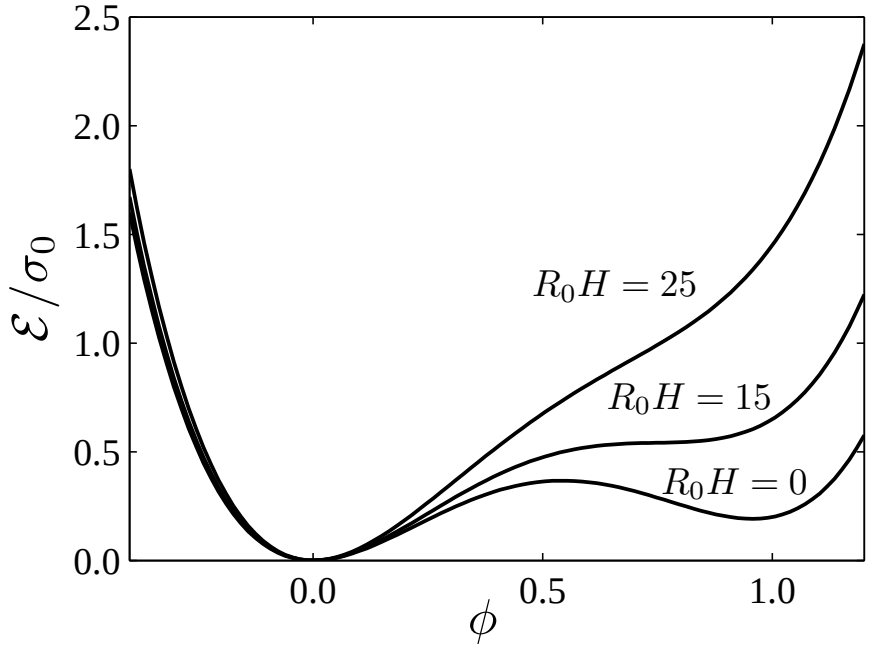

Figure 3.1: Dimensionless free energy density $\mathcal{E}/\sigma_0$ (up to additive constants) vs. ϕ, for various dimensionless mean curvatures R_0H. Increasing R_0H increases the potential energy for phase 2 relative to phase 1. Parameter values: $\alpha_1 = 0.2$, $\alpha_2 = 0.2$, $\kappa_0/\sigma_0 = 0.005R_0^2$, $\lambda/\sigma_0 = 10$, and ϕ is uniform.

The total free energy is $F = F_1 + F_2 = \int \mathcal{E} \mathrm{d}^2u$. Figure 3.1 illustrates the mechanism by which high curvature drives a transition from phase 2 to phase 1. For the parameter values given in the caption, phase 1 is slightly favored over phase 2 for a membrane with vanishing

mean curvature, $H = 0$. As the mean curvature increases, phase 2 is less and less favored until eventually phase 1 is the only equilibrium phase. Fixing the mean curvature and increasing tension has the same effect. To determine the condition for a single minimum, differentiate the energy density for uniform ϕ with respect to ϕ:

$$\frac{\partial \mathcal{E}}{\partial \phi} = \sqrt{g}\phi \left[\kappa_0 \alpha_1 (2H)^2 + 2\sigma_0 \alpha_2 + \lambda(1-\phi)(1-2\phi)\right]. \tag{3.3}$$

The potential has a single minimum at $\phi = 0$ if the term in brackets in Eq. (3.3) is positive for all ϕ. Minimizing this term over ϕ yields the final condition for a potential with a single minimum,

$$\kappa_0 \alpha_1 (2H)^2 + 2\sigma_0 \alpha_2 > \lambda/8. \tag{3.4}$$

Sufficiently high curvature or tension can drive a transition from the low-flexibility phase 2 to the high-flexibility phase 1.

3.1.3 Results and discussion

We now turn to the special case of membrane tubules. Suppose σ_0 is fixed, as in an experiment in which a tubule is pulled from a vesicle aspirated onto a pipet [33, 2]. Since the fully developed tubule is cylindrical, ϕ is uniform far enough away from phase boundaries. Thus, the tubule radius R and the equilibrium force f_t required to maintain the tubule are given by $R = \sqrt{\kappa_\beta/(2\sigma_\beta)}$ and $f_\mathrm{t} = 2\pi\sqrt{2\kappa_\beta\sigma_\beta}$ (see [70, 37], e.g.), where $\beta = 1$ or 2 depending on the phase in the tubule. For phase 1, $\kappa_1 = \kappa_0(1-\alpha_1)$ and $\sigma_1 = \sigma_0(1-\alpha_2)$. In phase 2, the equilibrium value of $\phi = \phi_1$ is shifted below unity by the coupling of ϕ

to curvature and tension (see Fig. 3.1). For $\phi_1 \approx 1$, we have $\kappa_1 \approx \kappa_0$ and $\sigma_1 \approx \sigma_0$. If the tubule curvature $2H = 1/R$ is large enough to satisfy the condition (3.4), then phase 2 is expelled from the tubule region, even if the vesicle is in phase 1. This situation was observed in the experiments of Roux et al. [2].

To discuss the formation of a tubule, recall the results of reference [70] for the case of a one-component membrane, in which the tubule is pulled not from a spherical vesicle but from a membrane disk held at constant tension. For small displacements, there is no tubule, and the membrane has a catenoidal shape except in a small region surrounding the point force. The catenoid has zero mean curvature and is therefore a minimal surface, with a shape governed by the tension term of the free energy. The small region surrounding the point force has $H \neq 0$ and a shape determined by a balance of the bending and tension terms. For sufficiently large displacement, this region elongates into a cylindrical tubule as in Fig. 3.2. To solve for the shape and composition of a tubule with our free energy F, we assume an axisymmetric shape and use cylindrical coordinates (r, θ, z), where z is the axis of symmetry of the tubule. Defining s as the arclength measured along a meridian with the point of application of the force as the origin, our surface coordinates are $\{u_1, u_2\} = \{s, \theta\}$, and the surface is $\mathbf{X}(s, \theta) = (r(s)\cos\theta, r(s)\sin\theta, z(s))$. Defining $\psi(s)$ as the angle between the tangent vector $\partial\mathbf{X}/\partial s$ and $\hat{\mathbf{r}}$ yields $\partial r/\partial s = \cos\psi$ and $\partial z/\partial s = -\sin\psi$. The metric tensor is diagonal with $g_{ss} = 1$ and $g_{\theta\theta} = r^2$, and the mean curvature is $H = (\partial\psi/\partial s + \sin\psi/r)/2$.

The Euler-Lagrange equations for F are obtained in the standard way and will not be displayed. The boundary conditions are $\psi(0) = 0$, $H(L) = 0$, $r(0) = 0$, $r(L) = 1$, $z(0) = z_0$ and $z(L) = 0$, where z_0 is the displacement of the tip of the tubule, measured

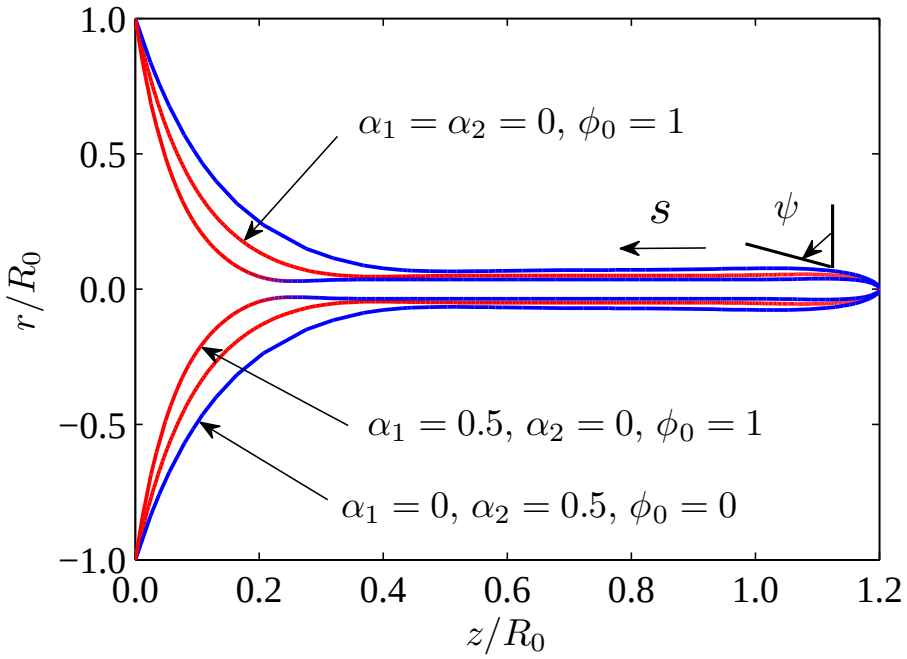

Figure 3.2: (Color online) Membrane shapes for displacement $z_0 = 1.2R_0$ and three different sets of coupling parameters. (i) No coupling: $\alpha_1 = \alpha_2 = 0$ and $\phi_0 = 1$; the entire membrane is in phase 2 (red). (ii) Coupling of composition and flexibility: $\alpha_1 = 0.5$, $\alpha_2 = 0$, and $\phi_0 = 1$. The catenoid is in phase 2 and the tubule is in phase 1 (blue). (iii) Coupling of composition and tension: $\alpha_1 = 0$, $\alpha_2 = 0.5$, and $\phi_0 = 0$. The entire membrane is in phase 1.

from the plane of the ring, and L is the unknown contour length of a meridian. The order parameter at $s = L$ is fixed to a constant, $\phi(L) = \phi_0$, since $s = L$ corresponds to a vesicle with a known composition. But the order parameter at $s = 0$ is free to vary, leading to the condition $\phi_s(0) = 0$. The unknown arclength and the singularities at $r = 0$ are handled exactly as in references [43, 32]. The equations are solved numerically with the parameter values corresponding to deep wells, $\lambda/\sigma_0 = 10$; sharp domain boundaries, $\mu/(\sigma_0 R_0^2) = 0.005$; and thin tubules, $\kappa_0/(\sigma_0 R_0^2) = 0.005$.

Figures 3.2 and 3.12 show the membrane shapes and force-vs.-extension curves for three different representative sets of coupling parameters. The baseline case has no coupling,

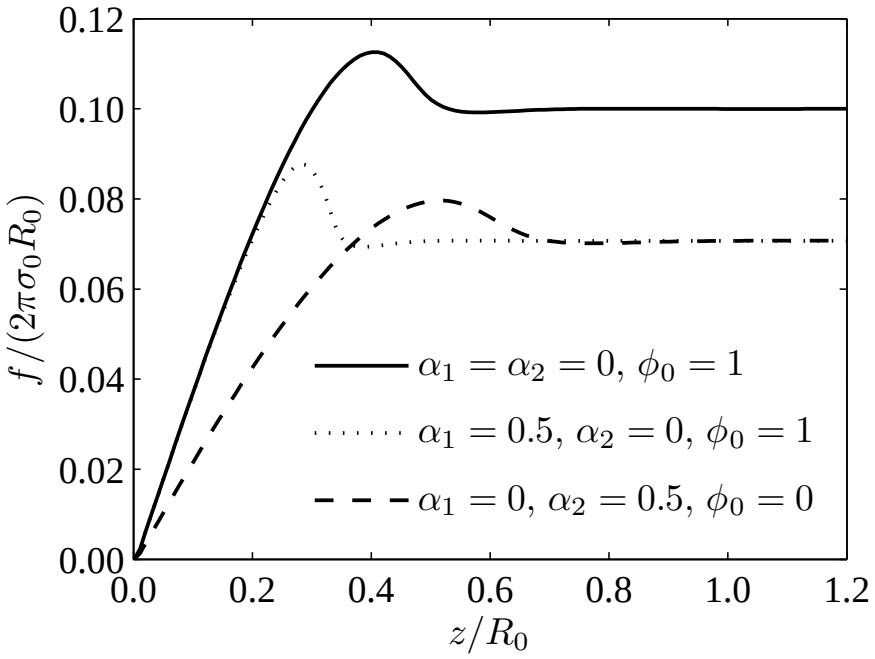

Figure 3.3: Dimensionless force $f/(2\pi\sigma_0 R_0)$ vs. dimensionless displacement z/R_0 for the three sets of coupling parameters of Fig. 3.2.

$\alpha_1 = \alpha_2 = 0$, and the entire membrane is in phase 2, with $\phi = 1$. For small displacement $z_0 \lesssim 0.2R_0$, the membrane is a catenoid for most of its surface, and the force is proportional to σ_0. As the displacement increases, the force rises to a maximum $f_{\max}$, and then decreases slightly to reach the plateau value $f_{\rm t} = 2\pi\sqrt{2\kappa_0\sigma_0}$. The force-extension curve for this case is the solid line of Fig. 3.12. Now consider the case of coupling between composition and bending only, $\alpha_1 = 0.5$ and $\alpha_2 = 0$, with the membrane disk in phase 2 when the displacement is zero. Since the mean curvature diverges logarithmically as $r \to 0$, there is always a small region in phase 1 surrounding the point of application of the force. The catenoidal region remains in phase 2, and there is a circular domain boundary separating the two phases. The force-extension curve in this case (dotted line, Fig. 3.12) initially follows the baseline case because there is no coupling to tension. For these parameters, the

mean curvature of a fully developed tubule is sufficiently high to eliminate the minimum in the potential corresponding to phase 2 (Fig. 3.1). Once the tubule forms, phase 1 spreads from the small region near the point force to the whole tubule. The shape and force depend continuously on displacement through this process. The force barrier and the plateau force f_t are smaller than the baseline case since phase 1 is more flexible than phase 2. Note also that the coupling α_1 affects the overshoot $(f_{max} - f_t)/f_t$. The final case, $\alpha_1 = 0$ and $\alpha_2 = 0.5$ illustrates the effect of the coupling between tension and composition. The membrane tension is effectively reduced by the factor $1 - \alpha_2$ relative to the baseline case, leading to a lower slope in the initial part of the force-extension curve, a lower plateau force (Fig. 3.12, dashed line), and a wider tubule (Fig. 3.2). Note that the barrier $f_{max} - f_t$ is greater for the dotted line ($\alpha_1 = 0.5$, $\alpha_2 = 0$, $\phi_0 = 1$) than for the dashed line ($\alpha_1 = 0$, $\alpha_2 = 0.5$, $\phi_0 = 0$) since in the former case, additional work must be done to overcome the potential barrier in the transition from phase 2 to phase 1 in the tubule.

When R^{-1} is low enough that $\mathcal{E}$ has two wells, tubule formation can occur by a discontinuous transition. Fig. 3.4 shows such a case for $\alpha_1 = \alpha_2 = 0.2$. As z/R_0 increases, the membrane shape and the position of the circular domain wall surrounding $s = 0$ change continuously. At the point D of the inset to Fig. 3.4a, two different branches of solutions have the same energy. We denote these branches as the catenoid branch and the tubule branch. Since the membrane shape and the position of the circular domain wall are different on the two branches, there is a discontinuity at the point D. A discontinuity in the force vs. extension curve similar to that in Fig. 3.4 has been observed in experiments [2, 92, 15]. One proposed explanation is the finite size of the attachment area of the membrane to the device that pulls out the tether [27]. Here we have shown that multicomponent membranes

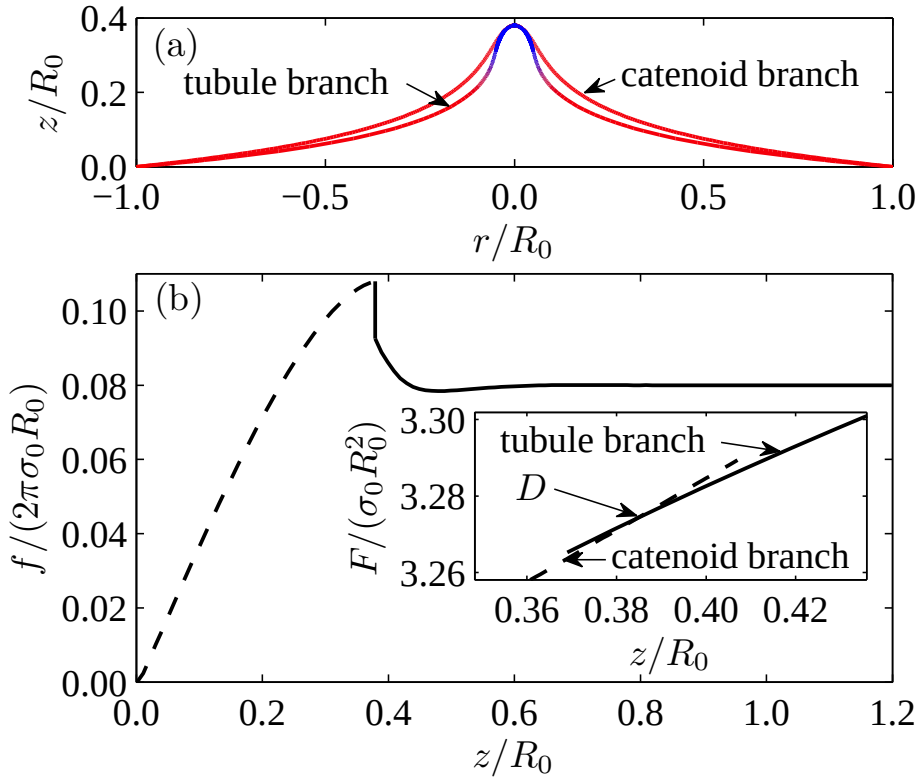

Figure 3.4: (a) (Color online) Membrane shapes for the two branches at D defined in (b). Blue is phase 1 and red is phase 2. (b) Dimensionless force $f/(2\pi\sigma_0 R_0)$ vs. dimensionless displacement z/R_0 for $\alpha_1 = \alpha_2 = 0.2$ with $\phi_0 = 1$. The inset shows the total dimensionless energy $F/(\sigma_0 R_0^2)$. The catenoid branch is a dashed line and the tubule branch is a solid line. The two branches of solutions cross at D.

can have a discontinuous force-extension curve even for a point force.

We have shown quantitatively how membrane curvature can sort lipids during tubule formation. Since the flexible phase generically segregates into the tubule region, the force required to maintain a tubule is reduced by the coupling of composition and flexibility. Our results show that the force barrier that must be surmounted is also reduced by this coupling. These results are consistent with the experimental findings of reference [2], in which almost every tubule formed was in the L_d phase. Our simple approach is most appropriate in situations where the mean curvature is high.

3.2 A new method to measure the line tension of lipid rafts

The line tension of lipid rafts plays an important role in the kinetics of phase separation and domain sizes. Usually, the line tension is measured by using micropipette aspiration [4]. It is also feasible to determine the line tension of a membrane raft using the tether pulling process. The line tension of the domain will affect the force-extension curve. The full curve and the effect of line tension must be calculated numerically. To get started on this problem, we consider the simpler problem of the effect of the line tension on the force-extension curve once the tubule has already formed, as in Fig.(3.5). That is, we consider the effect on the plateau pulling force. The variable R denotes the radius of the domain at the instant shown. The "similar regions" are regions that do not change their shape as the length of the tubule is slightly increased.

Focusing on the plateau pulling force has several advantages. First, it evades questions of the shape of the domain in the limit of zero force. Second, the detachment of the contact region between membrane and bead (just to the right of the tether, not shown) occurs during the pulling process. The effect of the detachment is relatively large before membrane tube formation, but not in the plateau region. Finally, the membrane shape remains similar after the membrane tube is formed and before the whole domain enter the membrane tube.

We separate the domain into two parts. One part does not change much during the extension, and the other is the cylindrical tube, which lengthens (Fig.(3.5)). The first part include catenoidal region and the cap region, as shown in Fig.(3.5). The energy of the first part remains constant since the shape doesn't change much. The energy of the tube part

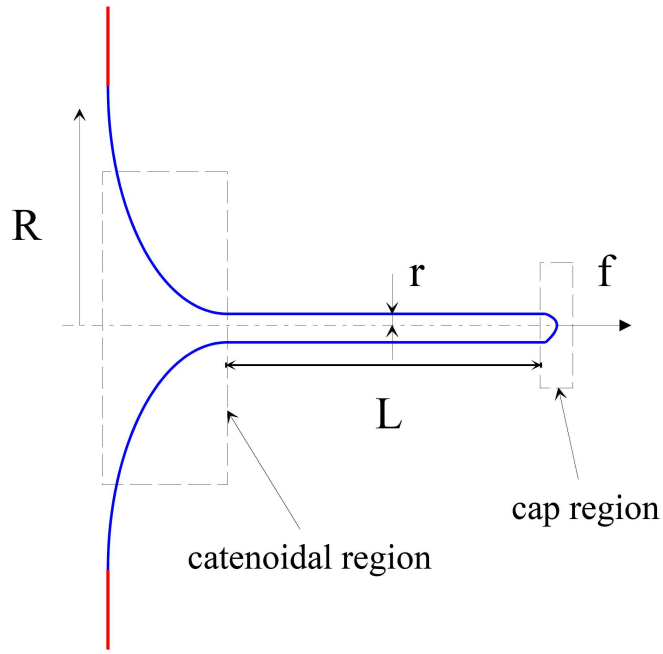

Figure 3.5: Pulling out a membrane tube from a lipid raft. Different colors represent different phases.

includes the bending energy and the surface energy. There are also some extra energies which result from the line tension and the external force. Therefore, the total energy of the system is

$$G = G_0 + \pi L\frac{\kappa}{r} + 2\pi rL\sigma - fL + 2\pi RT, \tag{3.5}$$

where G_0 is the roughly constant energy of the catenoidal region and the cap region. The constants κ, σ and T are bending stiffness, surface energy and line tension respectively. r is the radius of the membrane tube. R is the size of the raft. L is the length of the membrane tube. f is the applied pulling force. The total differential of G is

$$\begin{aligned} dG = \quad & (-\pi L\frac{\kappa}{r^2} + 2\pi L\sigma)dr \\ & +(\pi\frac{\kappa}{r} + 2\pi r\sigma - f)dL + 2\pi T dR, \end{aligned} \tag{3.6}$$

Assume the raft area is conserved. This means we have following relation

$$2\pi R dR = -2\pi r dL, \tag{3.7}$$

or

$$dR = \frac{r}{R} dL. \tag{3.8}$$

Combine Eqn.(3.6) and (3.8) and use the condition $dG = 0$ at equilibrium. The governing equations are obtained.

$$-\frac{\kappa}{2r^2} + \sigma = 0, \tag{3.9}$$

$$\pi\frac{\kappa}{r} + 2\pi r\sigma - f - 2\pi T\frac{r}{R} = 0. \tag{3.10}$$

Solving these equations, we get

$$r = \sqrt{\frac{\kappa}{2\sigma}}, \tag{3.11}$$

$$f = f_0 - 2\pi T\frac{r}{R}, \tag{3.12}$$

where f_0 is the plateau pulling force without the line tension and $f_0 = \frac{\kappa}{2}\frac{1}{r}2\pi + \sigma 2\pi r = 4\pi r\sigma$. The typical pulling force is showed in Fig.(3.6). We can see that the effect of the line tension is to decrease the the plateau pulling force. The smaller the domain size is, the smaller the pulling fore is. The limit case is that the domain is infinitely large, yielding the plateau pulling force for homogeneous membrane.

If the tubule radius, force, and domain radius can be measured for two different exten-

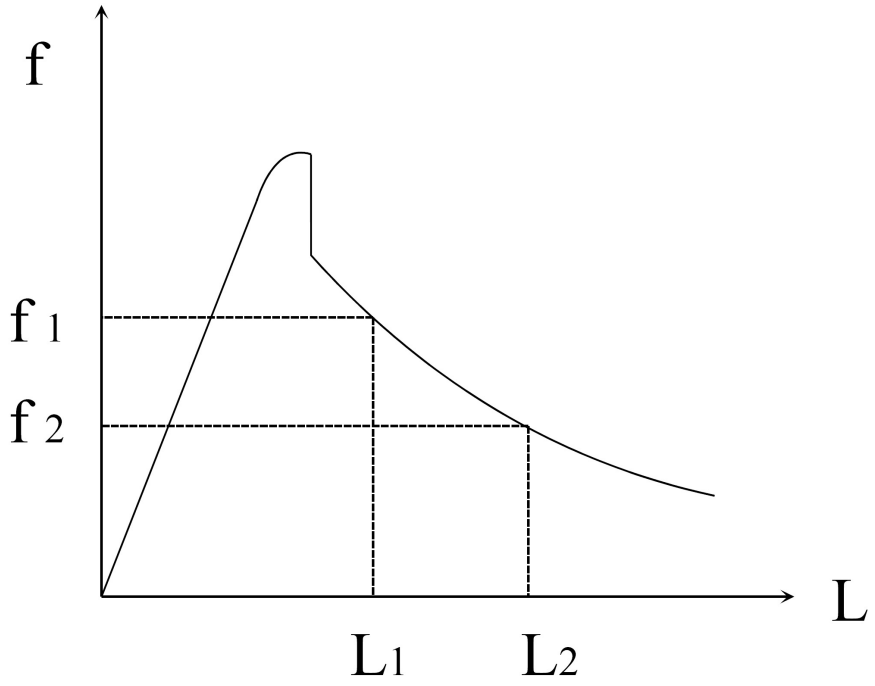

Figure 3.6: The pulling force

sions, the line tension may be determined from Eqn.(3.12)

$$f_2 - f_1 = -2\pi r T(\frac{1}{R2} - \frac{1}{R1}), \tag{3.13}$$

where f_1, f_2, R_1 and R_2 are the plateau pulling forces and domain radii at two different extensions. The advantage of this formula is that it only need the geometrical parameters r, R_1 and R_2 and the pulling forces f_1 and f_2; the bending stiffness κ and the surface energy σ are not required.

An interesting phenomena may occur for large line tension and small raft size. After overcoming a force barrier, the membrane tube could grow automatically (f=0) due to the line tension. The critical condition is $f_0 = 2\pi Tr/R$.

Our assumptions should be clearly stated. First, these calculations assume an intermediate domain size R. If the domain is too large, the line tension effect is small. On the other hand, if the domain is too small, it will be pulled into the tubule as the tubule extends, and a more detailed analysis is required. Second, the tubule must be pulled from the center of the domain since we assumed axisymmetry (unless the bead naturally migrates to the center to reduce energy). To decrease the effect of detachment between the bead and the membrane, the size of the bead should be as small as possible.

Chapter 4

Minimal Model for Hydrodynamic Synchronization of cilia

4.1 Introduction

One of the central aims in the field of cell motility is to understand how a collection of beating cilia coordinates, or, on a larger scale, how a collection of swimming organisms form coherent patterns. For example, the eukaryote *Paramecium* swims by propagating waves of ciliary beating along its surface [58]; how does this coordination arise? Likewise, sea urchin spermatozoa spontaneously form vortex patterns in the absence of any cell signaling [74]; what mechanism underlies this pattern formation? Coordination of cilia is also important in the transport of fluid. The coordination of nodal cilia in developing vertebrate embryos has been implicated in the determination of left-right asymmetry of the organism [67]. The cilia lining the human airway must beat in a coordinated manner to sweep foreign particles up the airway. Beating cilia may also play a role in the transport

of sperm and egg during fertilization in mammals [85].

These examples are instances of the general tendency for the emergence of synchronization in a broad array of physical and biological systems [68]. A long-standing hypothesis is that the coordination observed in nearby beating cilia or swimmers is due to hydrodynamic interactions between these objects [28, 82]. In recent years there have been many computational and theoretical studies to support this hypothesis [25, 29, 49, 48, 73, 52, 90, 31, 66]. The key physical fact underlying all of these studies is that at the small scale of the cell, where the Reynolds number Re is small, the velocity field arising from a deforming body falls off slowly with distance, leading to significant hydrodynamic forces between nearby bodies. Furthermore, the development of a fixed phase difference between two bodies—phase-locking—requires some kind of compliance in which the deforming body can adjust its beat pattern in response to hydrodynamic forces from other nearby bodies.

The nature of this compliance is subtle. In the case of two rotating rigid helices driven with fixed torques (the "deformation" here is rotation), the freedom of the phase of each helix to speed up or slow down to maintain the fixed torque for all phase differences does *not* lead to phase-locking [47]. Theoretical calculations suggest that additional degrees of freedom are required for phase-locking, or synchronization. For example, synchronization develops if the shafts of the rotating helices are connected to fixed points by stiff springs, allowing the helix axes to translate or tilt [73]. The directions of these small motions depend on whether the hydrodynamic forces are attractive or repulsive, which in turn depends in detail on the phase difference (cf. the case of nearby swimmers [5, 50]).

4.2 Experiments

The complexities of designing experiments that include both hydrodynamic interactions and controlled elastic deformation at very low Reynolds numbers have hindered experimental studies of hydrodynamic synchronization; therefore, we propose a scaled model system that captures the essential physics, allows for detailed measurements, and is amenable to modeling.

4.2.1 The experiment set up

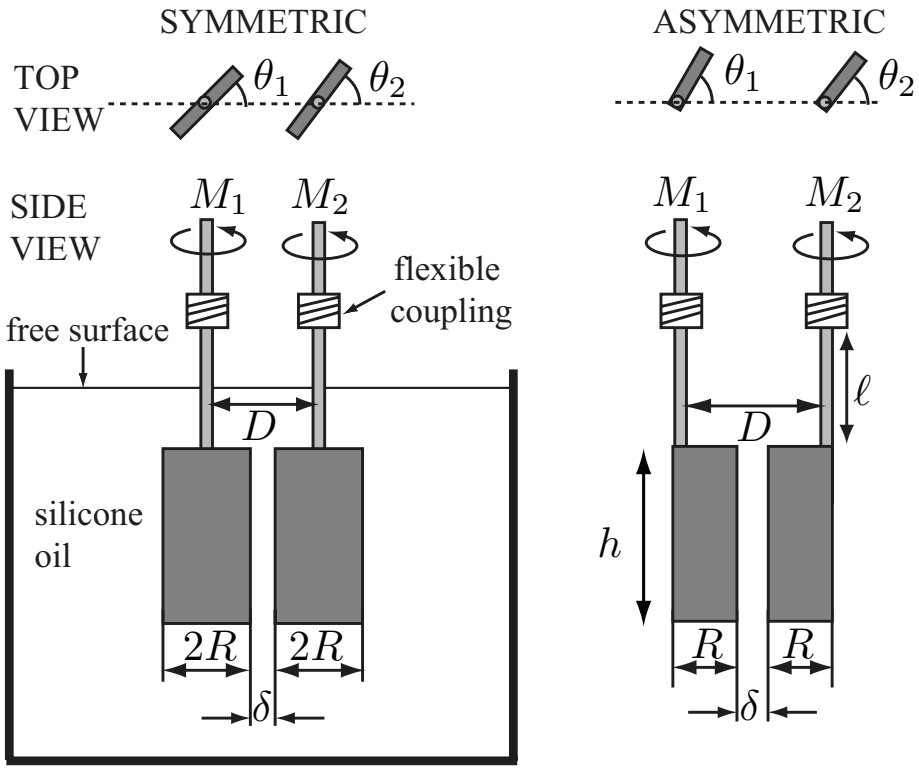

Figure 4.1: Schematic of the model system for hydrodynamic synchronization. Left: A pair of symmetric paddles in a fluid with viscosity η are rotated with constant torques M_1 and M_2. The shafts are rigid but have flexible couplings that allow the paddles to tilt. Right: asymmetric paddles.

Figure 4.1 illustrates the experimental configuration. Two thin paddles are immersed in a large tank filled with a viscous fluid ($\eta = 110\,\mathrm{Ns/m^2}$), separated at their closest approach by a small gap, $\delta = 3.6\,\mathrm{mm}$. We study two different paddle configurations: symmetric and asymmetric. The symmetric paddle has the axis of rotation through the paddle center and dimensions $h = 60\,\mathrm{mm}$, $w = 2R = 30\,\mathrm{mm}$, and thickness $t = 6\,\mathrm{mm}$. The asymmetric paddle has the axis of rotation through one edge and dimensions $60 \times 18 \times 6\,\mathrm{mm}$. The supporting shafts are hardened steel, of diameter $6.35\,\mathrm{mm}$ and length $\ell = 120\,\mathrm{mm}$ long, connected to the motors via flexible couplings that allow the paddles to tilt. The shafts are so rigid that bending due to hydrodynamic forces is negligible, but the couplings act as torsional springs with spring constant $k_\mathrm{T} = 8000\,\mathrm{mN\text{-}m/rad}$. This flexibility allows the paddles to tilt slightly in response to hydrodynamic forces. We also tested shafts without an intermediate coupling, in which the tilt of the paddles effectively vanished. The bearing assemblies are supported on separate stages to minimize any mechanical communication beyond hydrodynamic interactions [9], and to allow for precise control of the distance of closest approach, δ. Since $\delta/h << 1$, the resultant flow is mostly two-dimensional, in the plane perpendicular to the axes of rotation. The two paddles are driven at constant torque using a servo motor, digital encoder, and feedback controller. Typical driving torques, range from $4\,\mathrm{mN\text{-}m}$ to $25\,\mathrm{mN\text{-}m}$, yielding rotation frequencies no more than $0.2\,\mathrm{Hz}$. At these conditions, the Reynolds number is $Re = \rho\omega R^2/\eta \approx 10^{-3}$, small enough to justify the neglect of inertial forces.

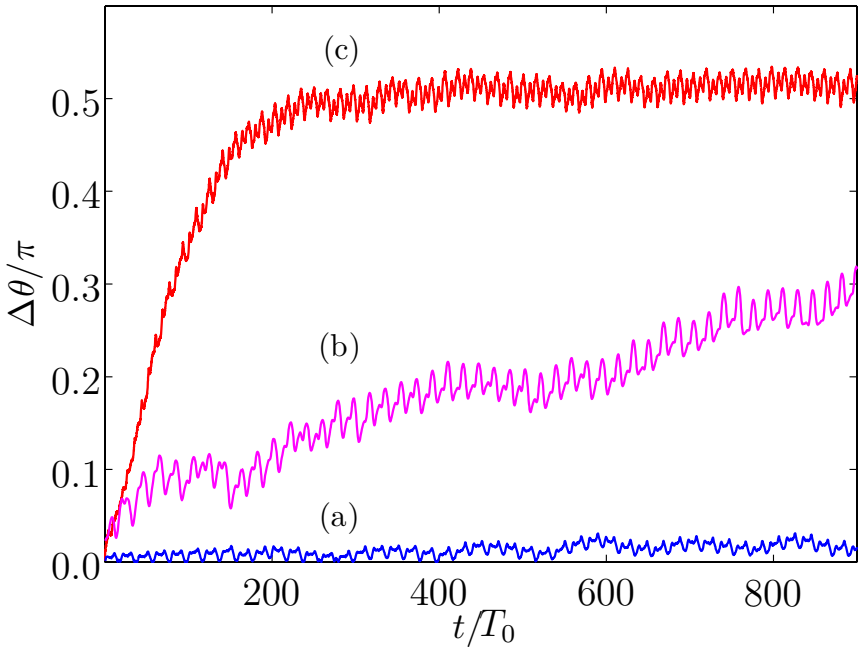

Figure 4.2: (Color online.) Phase difference $\Delta\theta = \theta_2 - \theta_1$ vs. dimensionless time t/T_0 ($T_0 = 6\pi\eta R^3/M$) for symmetric paddles with (a) $M_1 = M_2$ and stiff shafts, (b) $(M_2 - M_1)/M_1 \approx 0.003$ and stiff shafts, and (c) $M_1 = M_2$ and shafts with flexible couplers.

4.2.2 Experimental results

Since inertia is negligible, the characteristic velocities scale linearly with the motor torques (M_1, M_2), and thus the state of the system is determined by the angles of the two paddles (θ_1, θ_2) (Fig. 4.1) and the small shifts due to the flexible couplers. In the high-stiffness case, the paddles did not synchronize in any measurable time; instead, the phase of each paddle increased roughly linearly with driving torque, $(\theta_1, \theta_2) \propto (tM_1, tM_2)$, independent of the initial phase difference (Fig. 4.2a, b). However, paddles with flexible couplers and small distance of closest approach locked phases in 10–20 revolutions (Fig. 4.2c). Note that $\delta/R = 0.24$ for all experiments reported in this letter, and that we measure time in units of $T_0 = 6\pi\eta R^3/M$, (M is the mean torque) which is roughly one tenth of a rotation period. The tilted angle of shafts is showed in Fig 4.3. The wobble of the shaft for inflexible

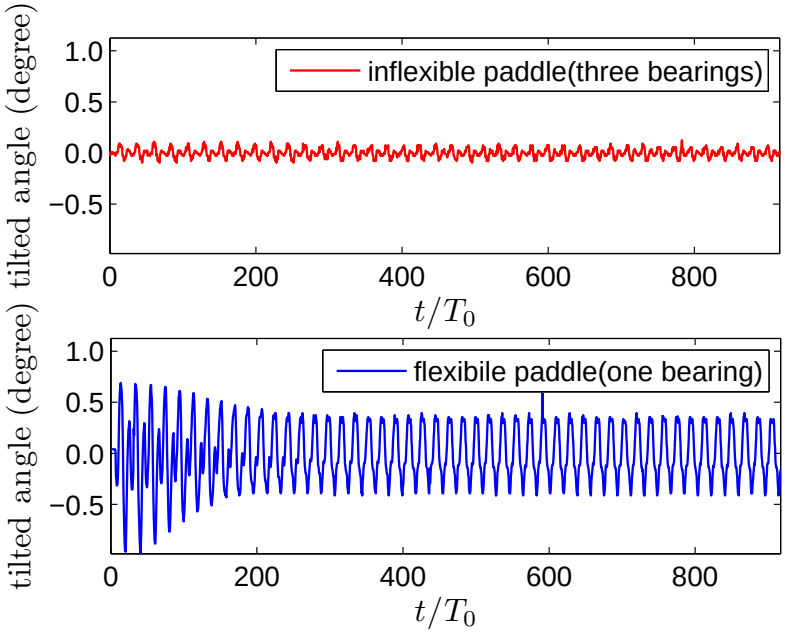

Figure 4.3: (Color online) The tilted angle vs. dimensionless time t/T_0 for symmetric paddles with flexible couplers (lower) and inflexible couplers (upper).

paddle is very small and the tilted angle is almost a constant in the experiment. While the wobble for flexible paddle is larger. But the tilted angle is still very small (less than 0.5° for symmetric paddle). The synchronization process is clearly seen in this case.

Several features of the synchronization are worth noting. For $M_1 = M_2$, the symmetric paddles locked phases at $\Delta\theta \equiv \theta_2 - \theta_1 = \pi/2$, and the asymmetric paddles settled at $\Delta\theta = 0$. These two states represent the conditions that roughly maximize the time the paddles spent in close proximity. Since the paddles would maximize the time spent close together if they maintained their typical initial phase differences ($\Delta\theta = 0$ for the symmetric paddles,

$\Delta\theta = \pi$ for the asymmetric paddles), the rotation speed of each paddle rises as the paddles synchronize. Denoting the rotation speed of an isolated paddle by ω_0, we found that the speed of both symmetric paddles rises from $0.72\omega_0$ to $0.85\omega_0$ as synchronization

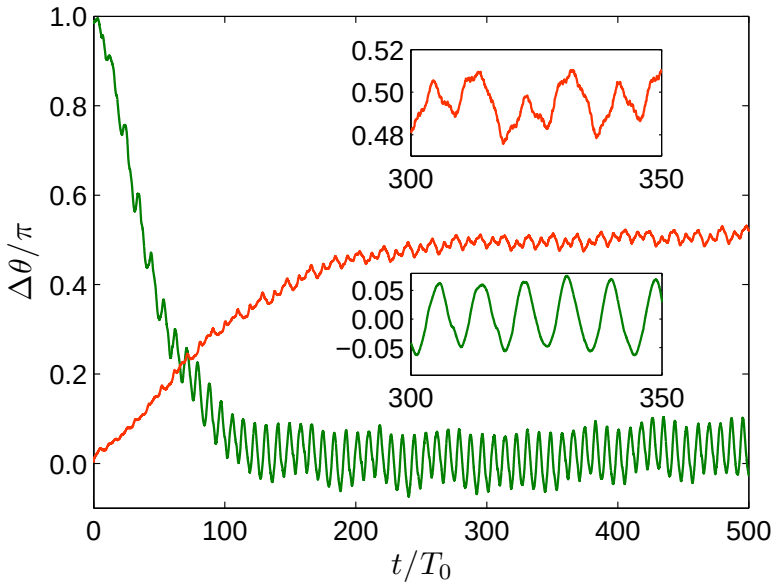

Figure 4.4: (Color online.) Phase difference vs. dimensionless time for symmetric (red line) and asymmetric paddles (green line). Time is measured in units of $T_0 = 6\pi\eta R^3/M$. The insets show the phase difference once phase-locking is achieved. In both cases, the normalized gap between the paddles is $\delta/R = 0.24$.

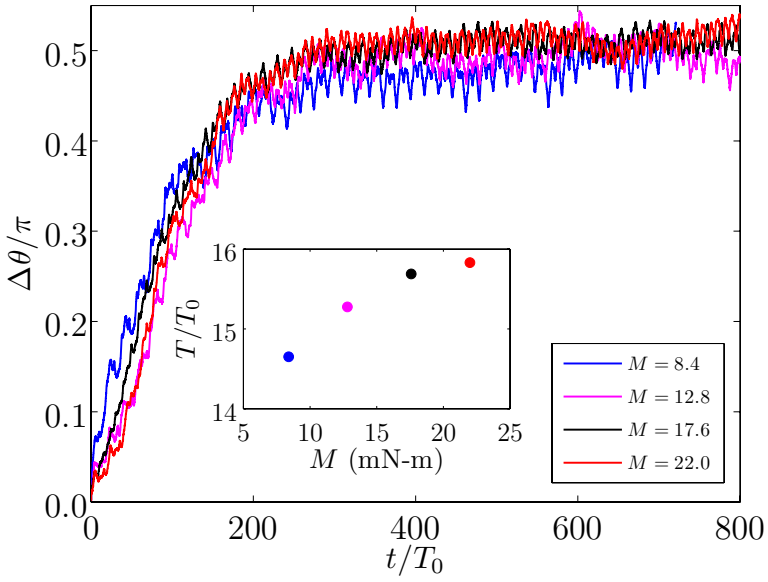

Figure 4.5: (Color online.) Phase difference vs. dimensionless time t/T_0 for symmetric paddles driven at torques $M_1 = M_2 = 8.4, 12.8, 17.5$, and 22 mN-m, with $\delta/R = 0.24$. The collapse of the data shows that the time to synchronize scales with $T_0 = 6\pi\eta R^3/M$. The inset shows the normalized rotation period T/T_0 vs. torque.

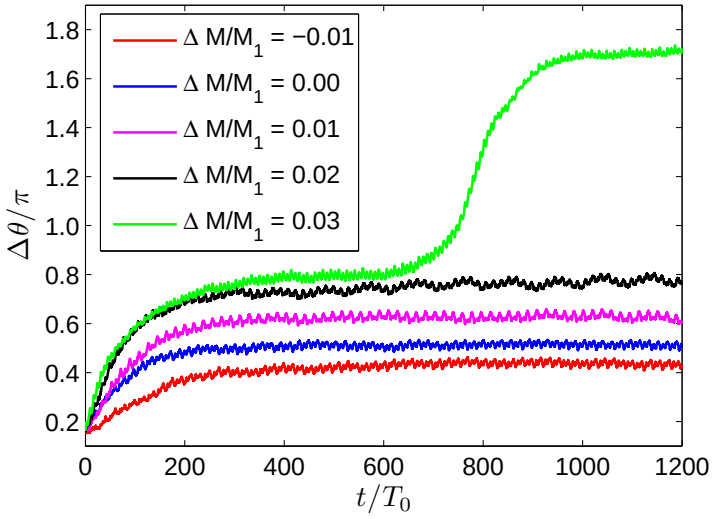

Figure 4.6: (Color online) Effect of torque mismatch on the synchronization for symmetric paddles at $\delta/R = 0.2$. Torque difference on two paddles $\Delta M = (M_2 - M_1)/M_1$ change by keeping M_1 and slightly varying M_2. As torque mismatches, paddles synchronize away from $\Delta\theta = \pi/2$ and further away with increasing torque difference. At large torque difference, the synchronization state become unstable and transition between synchronization states is observed.

develops, whereas the speed of both asymmetric paddles rises from $0.75\omega_0$ to $0.93\omega_0$. While these synchronized states are stable, there is a consistent and repeatable phase fluctuation (fig. 4.4-inset) corresponding to the variation in rotational speeds as the hydrodynamic interactions between the paddles wax and wane during a cycle. The fluctuation amplitude in the asymmetric case is larger than in the symmetric case because there is a larger variation in the distance between the asymmetric paddles during a period. These observations qualitatively agree with the results of numerical calculations on rotating rigid helices with flexible couplers [73]. In our experiments the phase fluctuations and rise in velocity as synchronization develops are more dramatic since the variation in the hydrodynamic interaction between paddles over a period is greater than in the case of helices.

The final state of synchronization was found to be independent of the initial orientation

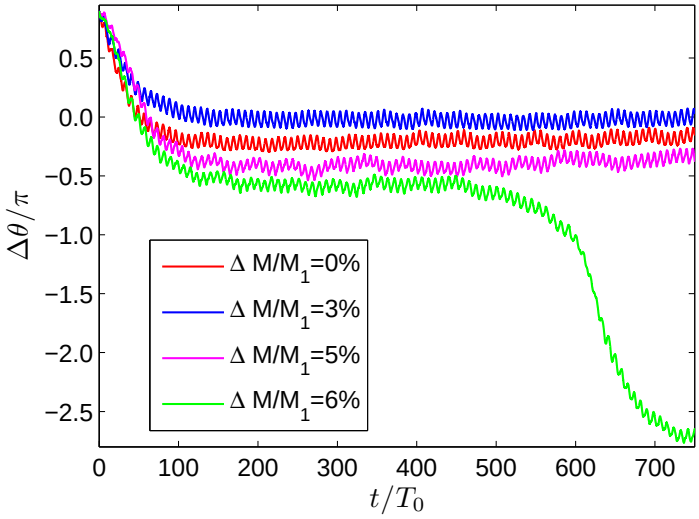

Figure 4.7: (Color online) Effect of torque mismatch on the synchronization for asymmetric paddles at $\delta/R = 0.2$. Torque difference on two paddles $\Delta M = (M_2 - M_1)/M_1$ change by keeping M_1 and slightly varying M_2. As torque mismatches, paddles synchronize away from $\Delta\theta = 0$ and further away with increasing torque difference. At large torque difference, the synchronization state become unstable and transition between synchronization states is observed.

of the paddles, and the time to synchronize scales with T_0, perhaps with a weak dependance on torque. (Figure 4.5). The number of paddle revolutions needed to synchronize is therefore roughly constant, 15 in the case of symmetric paddles, and 20 for asymmetric paddles. In the synchronized state, however, the rotation period T/T_0 does increase slightly with torque (Figure 4.5-inset).

When the paddles are operated with a torque mismatch between the two motors, the synchronized phase difference will deviate from $\pi/2$ (symmetric paddle) or 0 (asymmetric paddle). Although for a large mismatch, $\Delta M/M_1 = 3\%$ for symmetric paddle and $\Delta M/M_1 = 6\%$ for asymmetric paddle, the synchronized state is only marginally stable and the phase difference can jump abruptly by $\Delta\theta = \pi$ for symmetric paddle (Fig. 4.6) and $\Delta\theta = 2\pi$ for asymmetric paddle (Fig. 4.7).

4.3 Simulation

These experiments give strong evidence that the phase-locking of the paddles is due to hydrodynamic interactions. To further understand how hydrodynamic interaction cause the paddles to entrain, numerical simulations were performed with regularized stokeslests method [14, 71]. To make the thesis self-contained, firstly I review the Stokes flow and the method of regularized stokeslets.

4.3.1 The Method of Regularized stokeslets

If Reynolds number is low, i.e. $Re \ll 1$, the Navier-Stokes equations are reduced to the Stokes equations. In this case, the inertial forces are very small compared with viscous forces. Therefore the inertial terms in Navier-Stokes equations are negligible. This is a typical situation when the velocities of the fluid are very slow, the viscosities of the fluid are very large, or the length-scales of the flow are very small.

The Stokes equations are

$$\eta \Delta \mathbf{u} - \nabla p = -\mathbf{F}, \tag{4.1}$$

$$\nabla \cdot \mathbf{u} = 0, \tag{4.2}$$

where η is the dynamic viscosity, $\mathbf{u}$ is the velocity, p is the pressure, and $\mathbf{F}$ is the applied body force. The Green function for Stokes equation can be found due to the linearity of the equation. The solution is also called Stokeslet. Suppose a concentrated external force is applied in the fluid, i.e. $\mathbf{g}\delta(\mathbf{x} - \mathbf{x}_0)$. Then the velocity $u_i(\mathbf{x})$, pressure $p(\mathbf{x})$ and stress

tensor $\sigma_{ik}(\mathbf{x})$ of the flow are

$$u_i(\mathbf{x}) = S_{ij}(\mathbf{x}, \mathbf{x}_0) g_j, \tag{4.3}$$

$$p(\mathbf{x}) = P_j(\mathbf{x}, \mathbf{x}_0) g_j, \tag{4.4}$$

$$\sigma_{ik}(\mathbf{x}) = T_{ijk}(\mathbf{x}, \mathbf{x}_0) g_j, \tag{4.5}$$

where $r = |\mathbf{x} - \mathbf{x}_0|$ and

$$S_{ij}(\mathbf{x}, \mathbf{x}_0) = \frac{1}{8\pi\eta}[\frac{\delta_{ij}}{r} + \frac{(x_i - x_{0,i})(x_j - x_{0,j})}{r^3}], \tag{4.6}$$

$$P_j(\mathbf{x}, \mathbf{x}_0) = \frac{(x_i - x_{0,i})}{4\pi r^3}, \tag{4.7}$$

$$T_{ijk}(\mathbf{x}, \mathbf{x}_0) = -\frac{3(x_i - x_{0,i})(x_j - x_{0,j})(x_k - x_{0,k})}{4\pi r^5}. \tag{4.8}$$

$S_{ij}(\mathbf{x}, \mathbf{x}_0)$ is a second rank tensor known as the Oseen tensor [21]. More complicated problems can be solved by the superposition of stokeslets. For example, slender body theories![46, 53, 30] use the slenderness of a body and the superposition of stokeslets to solve the velocity and pressure fields around the body. This technique is widely used on the motion of flagellar [36, 35, 54] The solution for a distributed force density $\mathbf{f}(\mathbf{x})$ is

$$u_i(\mathbf{x}) = \int S_{ij}(\mathbf{x}, \mathbf{x}_0) f_j(\mathbf{x}_0)\, d\mathbf{x}_0, \tag{4.9}$$

$$p(\mathbf{x}) = \int P_j(\mathbf{x}, \mathbf{x}_0) f_j(\mathbf{x}_0)\, d\mathbf{x}_0, \tag{4.10}$$

$$\sigma_{ik}(\mathbf{x}) = \int T_{ijk}(\mathbf{x}, \mathbf{x}_0) f_j(\mathbf{x}_0)\, d\mathbf{x}_0. \tag{4.11}$$

where $r = |\mathbf{x} - \mathbf{y}|$.

The singularity in the Stokeslet (Eqn.(4.6)) is proportional to $1/r$. To avoid the singularity, Cortez [14, 71] introduced a cutoff function to approximate the delta distribution. This method is called regularized stokeslets method. The governing equations of Stokeslet is modified as

$$\eta \Delta \mathbf{u} - \nabla p = -\mathbf{g}\phi_\epsilon(\mathbf{x} - \mathbf{x_0}) \tag{4.12}$$

$$\nabla \cdot \mathbf{u} = 0 \tag{4.13}$$

where $\phi_\epsilon(\mathbf{x} - \mathbf{x}_0)$ is the cutoff function which is the approximation to delta function. In the simulation, we use the following cutoff function,

$$\phi_\epsilon(\mathbf{x} - \mathbf{x}_0) = \frac{15\epsilon^4}{8\pi(r^2 + \epsilon^2)^{7/2}} \tag{4.14}$$

where $r = \|\mathbf{x} - \mathbf{x}_0\|$. With this choice, the solution of (4.12) and (4.13) is

$$u_i(\mathbf{x}) = S_{ij}^\epsilon(\mathbf{x}, \mathbf{x}_0) g_j, \tag{4.15}$$

$$p(\mathbf{x}) = P_j^\epsilon(\mathbf{x}, \mathbf{x}_0) g_j, \tag{4.16}$$

$$\sigma_{ik}(\mathbf{x}) = T_{ijk}^\epsilon(\mathbf{x}, \mathbf{x}_0) g_j, \tag{4.17}$$

where

$$P_j^\epsilon(\mathbf{x},\mathbf{x}_0) = \frac{1}{8\pi}[(x_j - x_{0,j})\frac{2r^2+5\epsilon^2}{(r^2+\epsilon^2)^{5/2}}], \tag{4.18}$$

$$S_{ij}^\epsilon(\mathbf{x},\mathbf{x}_0) = \frac{1}{8\pi\eta}[\delta_{ij}\frac{r^2+2\epsilon^2}{(r^2+\epsilon^2)^{3/2}} + \frac{(x_i - x_{0,i})(x_j - x_{0,j})}{(r^2+\epsilon^2)^{3/2}}], \tag{4.19}$$

$$T_{ijk}^\epsilon(\mathbf{x},\mathbf{x}_0) = \frac{1}{8\pi}\{-\frac{6(x_i - x_{0,i})(x_j - x_{0,j})(x_k - x_{0,k})}{(r^2+\epsilon^2)^{5/2}}$$
$$-\frac{3\epsilon^2[(x_i - x_{0,i})\delta_{jk} + (x_j - x_{0,j})\delta_{ik} + (x_k - x_{0,k})\delta ij]}{(r^2+\epsilon^2)^{5/2}}\}. \tag{4.20}$$

The regularized stokeslets method is the generalization of the Green function method for solving Stokes equations. It only modifies the singular solution in the near field, while the modification is negligible in the far field, i.e. $r \ll \epsilon$. The cutoff function $\phi_\epsilon(\mathbf{x} - \mathbf{x}_0)$ approaches to a delta function as $\epsilon \to 0$ and the regularized solutions is reduced to the singular Green function.

$$S_{ij}^\epsilon(\mathbf{x},\mathbf{x}_0) \to S_{ij}(\mathbf{x},\mathbf{x}_0), \tag{4.21}$$

$$P_j^\epsilon(\mathbf{x},\mathbf{x}_0) \to P_j(\mathbf{x},\mathbf{x}_0), \tag{4.22}$$

$$T_{ijk}^\epsilon(\mathbf{x},\mathbf{x}_0) \to T_{ijk}(\mathbf{x},\mathbf{x}_0). \tag{4.23}$$

4.3.2 The Simulation Method

Now we model two rectangular paddles driven by prescribed torque in a viscous fluid. The goal is to understand how hydrodynamic interactions cause the paddles to entrain. A simple approach is to replace each paddle with a rectangular array of closely spaced balls as shown in Fig.(4.8), and consider only the leading order hydrodynamic interactions among the balls. Each paddle has $N = N_1 N_2$ balls. The side of the paddle parallel to the

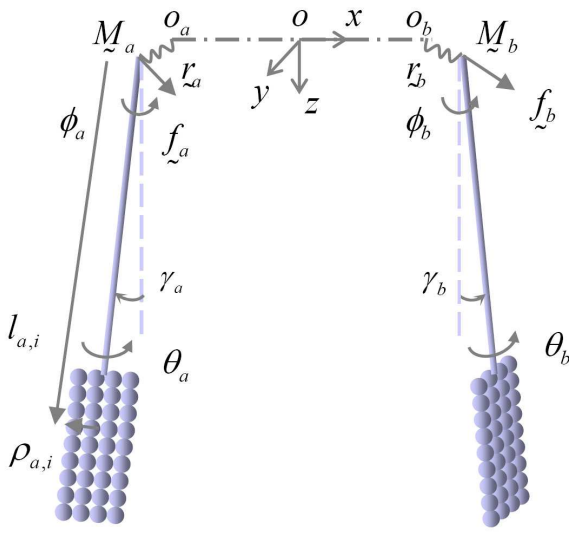

Figure 4.8: The configuration used in simulation. The tilt direction is represented by (γ, ϕ) and the rotation angle is θ. The paddle is replaced by an array of balls.

axis of rotation, taken to be the z axis, has N_1 balls. The other side has N_2 balls. The size is $2R \times 4R$ for symmetric paddle and $R \times 4R$ for asymmetric paddle. The distance between the two parallel axes is $2h$. Each paddle is connected to a rigid shaft, which is driven by a constant torque. The length of the shaft is l_0. The flexibility required for phase locking is controlled by the bearings that support each rotating shaft. The end of the shaft is connected to a fixed point by a regular spring with spring constant k. The force applied on the shaft is

$$\mathbf{f} = -k\mathbf{r}_\alpha = -k(x_\alpha, y_\alpha, z_\alpha) \tag{4.24}$$

where $\alpha = a, b$ labels the different paddles. The shaft can also tilt relative to z axis. The tilt angle is very small (less than 0.5° in the experiments). So we model the resistance to the tilt as a torsional spring with spring constant k_{tor}, which induces a torque that is

linear to the tilt angle. The total torque applied on the shaft is

$$\mathbf{M} = (k_{tor}\gamma \sin\phi, -k_{tor}\gamma\cos\phi, M_0) \tag{4.25}$$

where M_0 is the constant torque provided by the motor and (γ, ϕ) denote the orientation of shaft as shown in Figure (4.8). We found that the motion of shaft end is very small. So it's reasonable to assume $kR^2 \gg k_{tor}$. The position of each ball is:

$$\begin{aligned} \mathbf{x}_{\alpha,i} &= \mathbf{o}_\alpha + \mathbf{r}_\alpha + l_{\alpha,i}(\sin\gamma_\alpha\cos\phi_\alpha, \sin\gamma_\alpha\sin\phi_\alpha, \cos\gamma_\alpha) \\ &\quad +\rho_{\alpha,i}(\cos\theta_\alpha\cos\gamma_\alpha, \sin\theta_\alpha\cos\gamma_\alpha, -\sin\gamma_\alpha\cos(\phi_\alpha - \theta_\alpha)) \end{aligned} \tag{4.26}$$

where $i = 1, ..., N$ indicate the ith ball in each paddle and $\mathbf{o}_\alpha = (\mp h, 0, 0)$ for $\alpha = a$ or b. $l_{\alpha,i}$ and $\rho_{\alpha,i}$ are the position of the ith ball in local coordinates (see Fig. (4.8)). So the velocity of each ball is

$$\begin{aligned} \mathbf{v}_{\alpha,i} &= \frac{d\mathbf{x}_{\alpha,i}}{dt} \\ &= (\dot{x}_\alpha + l_{\alpha,i}\cos\gamma_\alpha\cos\phi_\alpha - \rho_{\alpha,i}\cos\theta_\alpha\sin\gamma_\alpha, \dot{y}_\alpha + l_{\alpha,i}\cos\gamma_\alpha\sin\phi_\alpha - \rho_{\alpha,i}\sin\theta_\alpha\sin\gamma_\alpha, \\ &\quad \dot{z}_\alpha + l_{\alpha,i}\sin\gamma_\alpha - \rho_{\alpha,i}\cos\gamma_\alpha\cos(\phi_\alpha - \theta_\alpha)) \end{aligned} \tag{4.27}$$

For the balls to move in the viscous fluid, they must be subjected to forces. The Oseen tensor gives the leading order (in inverse distance) dependence of the velocity of the fluid at a given point in terms of the force acting at a point, as shown in Eqn. (4.6). The approach is powerful and has been used for flexible filaments [56]. However, the Oseen

tensor is singular as r approaches to 0. In our simulation, we use another way, regularized stokeslets method as we introduced in last section, to avoid the singularity. Modify Eqn. (4.15) to include the effect of multiple stokeslets, the relation between the velocity $\mathbf{v}_i$ of the nth stokeslets and the forces $\mathbf{F}_j$ on all the stokeslets is

$$\mathbf{u}_m = \frac{\mathbf{F_m}}{6\pi\eta a} + \sum_{n\neq m} \mathbf{S}^{\epsilon}(\mathbf{x}_m, \mathbf{x}_n)\mathbf{F}_n, \tag{4.28}$$

where $\mathbf{u}_m$ and $\mathbf{F}_n$ are the displacement and the force applied at $\mathbf{x}_n$ respectively.

The balances of linear momentum and angular momentum of each paddle yield

$$-k\mathbf{r_a} - \sum_{n=1}^{N} \mathbf{F_n} = 0 \tag{4.29}$$

$$-k\mathbf{r_b} - \sum_{n=N+1}^{2N} \mathbf{F_n} = 0 \tag{4.30}$$

$$\mathbf{M_a} - \sum_{n=1}^{N} \mathbf{r_n} \times \mathbf{F_n} = 0 \tag{4.31}$$

$$\mathbf{M_b} - \sum_{n=N+1}^{2N} \mathbf{r_n} \times \mathbf{F_n} = 0 \tag{4.32}$$

4.3.3 Results and Discussions

In simulation, the radius a of the ball is 3 mm, which is one half of the thickness of the paddle. To get the same paddle size as the experiments, we use $N = 6 \times 11$ balls for symmetric paddles and $N = 4 \times 11$ for asymmetric paddles. The parameter ϵ in regularized stokeslets S_{ij}^{ϵ} is determined by the average rotation speed of the paddle in the experiments. ϵ is taken to be $1.15a$ and $1.5a$ for symmetric paddles and asymmetric paddles respectively. From the experiments we see that the main flexibility of the paddle is the tilt of the shaft.

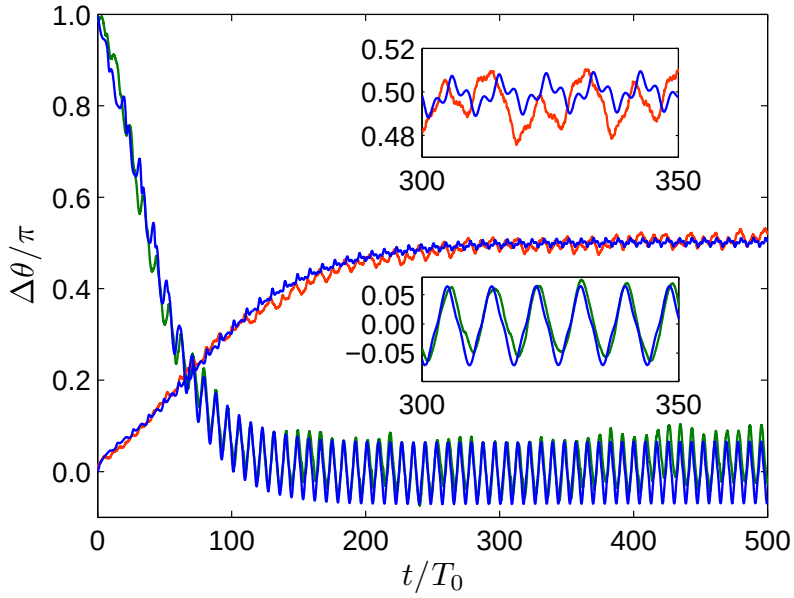

Figure 4.9: (Color online.) Phase difference vs. dimensionless time for symmetric (red line) and asymmetric paddles (green line), compared to simulation (blue lines). Time is measured in units of $T_0 = 6\pi\eta R^3/M$. The insets show the phase difference once phase-locking is achieved. In both cases, the normalized gap between the paddles is $\delta/R = 0.24$.

So it's reasonable to assume $kR^2 \gg k_{tor}$. In the calculation, the regular spring constant k is taken to be a very large number $10^4 M_0/R^2$ for both paddle configurations. We take $k_{tor} = 200M_0$ for symmetric paddles, and $k_{tor} = 600M_0$ for asymmetric paddles. These values of k_{tor} are consistent with the measured range in experiments.

Figure 4.9 shows the excellent agreement between the experiments and the simulations for both the asymmetric and the symmetric paddles. The simulation accurately captures the frequency and amplitude of the oscillations associated with the rotation of the motors, as well as the slower evolution of the phase-locking. When the driving torque is varied over the range used in the experiment, the simulations yield that the dimensionless time to synchronize T_s/T_0 remains approximately constant, with a weak dependence on torque, in accord with Fig. 4.5. Simulations with infinite spring constants k_{tor} and k show no phase-

locking. Since the paddles in the simulation are coupled only through the hydrodynamic interaction, we conclude that the cause of the phase-locking is the hydrodynamic interaction and not any stray mechanical coupling present in the experimental apparatus.

4.4 Theoretical Model

We can gain more insight into the mechanism of phase-locking by developing a simple theory along the lines of reference [66]. In the following section, I'll discuss the asymmetric and symmetric case respectively.

4.4.1 Asymmetric case

The absolute minimal model for the asymmetric paddles is to replace each paddle with a ball of radius a that travels on an orbit of radius R, driven by moment M. If the ball departs from this orbit, there is a linear restoring force in the radial direction, with spring constant k. The positions of the balls are

$$\mathbf{x}_1 = (-h/2 + x_a + R\cos\theta_a, y_a + R\sin\theta_a), \tag{4.33}$$

$$\mathbf{x}_2 = (h/2 + x_b + R\cos\theta_b, y_b + R, \sin\theta_b) \tag{4.34}$$

where $\mathbf{r}_a = (x_a, y_a)$ and $\mathbf{r}_b = (x_b, y_b)$ are the positions of the axes of rotation. h and R are constants which represent the separation of the fixed ends of the springs and the radius of rotation respectively. Here we use a and b to denote the axes of rotation, and use 1 and 2 to denote the balls. The use of different notations for the rotational axes and balls will be very convenient in the symmetric case. The velocities of the balls are $\mathbf{v}_i = \dot{\mathbf{x}}_i$.

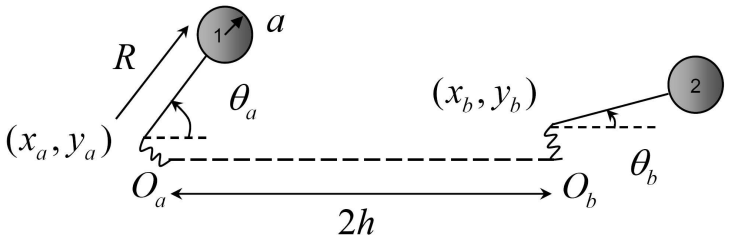

Figure 4.10: Minimal model for asymmetric paddles.

We use the Oseen tensor in Eqn. (4.6) to describe the hydrodynamic interaction between two balls. So the dependence of the velocity of the ith ball in terms of the forces acting at each ball is

$$\mathbf{v}_i = \frac{\mathbf{F}_i}{6\pi\eta a} + \frac{1}{8\pi\eta}\sum_{i\neq j}\left[\frac{\mathbf{F}_j}{r_{ij}} + \frac{\mathbf{F}_j\cdot\mathbf{r}_{ij}\mathbf{r}_{ij}}{r_{ij}^3}\right], \tag{4.35}$$

where $\mathbf{v}_i$ and -$\mathbf{F}_i$ are the velocity and the hydrodynamic force applied on the ith ball. $\mathbf{r}_{ij} = \mathbf{x}_j - \mathbf{x}_i$ and $r_{ij} = \|\mathbf{x}_j - \mathbf{x}_i\|$. Notice that the inertia is negligible when the Reynolds number is very small. So we only have the balance of the forces and the balance of the moments. And the origin of moments is arbitrary.

$$-k_a x_a - F_{1x} = 0, \tag{4.36}$$

$$-k_a y_a - F_{1y} = 0, \tag{4.37}$$

$$-k_b x_b - F_{2x} = 0, \tag{4.38}$$

$$-k_b y_b - F_{2y} = 0, \tag{4.39}$$

$$F_{1x}R\sin\theta_a - F_{1y}R\cos\theta_a + M_a = 0, \tag{4.40}$$

$$F_{2x}R\sin\theta_b - F_{2y}R\cos\theta_b + M_b = 0, \tag{4.41}$$

where F_{ix} and F_{iy} are the x and y components of $\mathbf{F}_i$ ($i = 1$ or 2). k_a and k_b are the spring

constants. M_a and M_b are the torques applied on the balls by the motors. Combining Eqn.(4.35) and Eqn. (4.36)-(4.41), we have

$$\dot{x}_a - \dot{\theta}_a R\sin\theta_a = -\frac{k_a x_a}{6\pi\eta a} + \frac{1}{8\pi\eta}\left[\frac{-k_b x_b}{r_{ab}} + \frac{(-k_b\mathbf{r}_b\cdot\mathbf{r}_{12})(\mathbf{r}_{12}\cdot\hat{x})}{r_{12}^3}\right], \tag{4.42}$$

$$\dot{y}_a + \dot{\theta}_a R\cos\theta_a = -\frac{k_a y_a}{6\pi\eta a} + \frac{1}{8\pi\eta}\left[\frac{-k_b y_b}{r_{ab}} + \frac{(-k_b\mathbf{r}_b\cdot\mathbf{r}_{12})(\mathbf{r}_{12}\cdot\hat{y})}{r_{12}^3}\right], \tag{4.43}$$

$$\dot{x}_b - \dot{\theta}_b R\sin\theta_b = -\frac{k_b x_b}{6\pi\eta a} + \frac{1}{8\pi\eta}\left[\frac{-k_a x_a}{r_{ab}} + \frac{(-k_a\mathbf{r}_a\cdot\mathbf{r}_{12})(\mathbf{r}_{12}\cdot\hat{x})}{r_{12}^3}\right], \tag{4.44}$$

$$\dot{y}_b + \dot{\theta}_b R\cos\theta_b = -\frac{k_b y_b}{6\pi\eta a} + \frac{1}{8\pi\eta}\left[\frac{-k_a y_a}{r_{12}} + \frac{(-k_a\mathbf{r}_a\cdot\mathbf{r}_{12})(\mathbf{r}_{12}\cdot\hat{y})}{r_{12}^3}\right], \tag{4.45}$$

$$-k_a x_a R\sin\theta_a + k_a y_a R\cos\theta_a + M_a = 0, \tag{4.46}$$

$$-k_b x_b R\sin\theta_b + k_b y_b R\cos\theta_b + M_b = 0. \tag{4.47}$$

Assume $k_a = k_b$ and define the length scale R, time scale $T_0 = 6\pi\eta R^3/M_a$, dimensionless quantity $\epsilon_T = M_a/(k_a R^2)$ and $\epsilon_L = R/h$. Here we use the far field approximation, i.e. $\epsilon_L \ll 1$, and only keep the leading terms of ϵ_L in equations (4.42)-(4.47). For example, $\frac{(-k_b\mathbf{r}_b\cdot\mathbf{r}_{12})(\mathbf{r}_{12}\cdot\hat{x})}{r_{12}^3} = \frac{q\epsilon_L}{\epsilon_T}x_b + O(\epsilon_L^2)$. The equations (4.42)-(4.47) are reduced to

$$\dot{x}_a - \dot{\theta}_a\sin\theta_a = -\frac{p}{\epsilon_T}x_a - \frac{q\epsilon_L}{\epsilon_T}2x_b, \tag{4.48}$$

$$\dot{y}_a + \dot{\theta}_a\cos\theta_a = -\frac{p}{\epsilon_T}y_a - \frac{q\epsilon_L}{\epsilon_T}y_b, \tag{4.49}$$

$$\dot{x}_b - \dot{\theta}_b\sin\theta_b = -\frac{p}{\epsilon_T}x_b - \frac{q\epsilon_L}{\epsilon_T}2x_a, \tag{4.50}$$

$$\dot{y}_b + \dot{\theta}_b\cos\theta_b = -\frac{p}{\epsilon_T}y_b - \frac{q\epsilon_L}{\epsilon_T}y_a, \tag{4.51}$$

$$-x_a\sin\theta_a + y_a\cos\theta_a + \epsilon_T = 0, \tag{4.52}$$

$$-x_b\sin\theta_b + y_b\cos\theta_b + \epsilon_T(1+\gamma_M) = 0, \tag{4.53}$$

where $p = R/a$, $q = 3/4$ and $\gamma_M = M_b/M_a - 1$. The equations (4.48)-(4.53) looks simple, but they still cannot be solved analytically. To simplify the problem further, we change variables. Define average phase angle $\bar{\theta} = \frac{1}{2}(\theta_a + \theta_b) = \omega t$ and phase difference $\Delta\theta = \theta_a - \theta_b$, where $\omega = \frac{d\bar{\theta}}{dt}$ is the average rotation speed. So we have

$$\dot{x}_a - (\omega + \Delta\dot{\theta}/2)\sin(\omega t + \Delta\theta/2) = -\frac{p}{\epsilon_T}x_a - \frac{q\epsilon_L}{\epsilon_T}2x_b, \tag{4.54}$$

$$\dot{y}_a + (\omega + \Delta\dot{\theta}/2)\cos(\omega t + \Delta\theta/2) = -\frac{p}{\epsilon_T}y_a - \frac{q\epsilon_L}{\epsilon_T}y_b, \tag{4.55}$$

$$\dot{x}_b - (\omega - \Delta\dot{\theta}/2)\sin(\omega t - \Delta\theta/2) = -\frac{p}{\epsilon_T}x_b - \frac{q\epsilon_L}{\epsilon_T}2x_a, \tag{4.56}$$

$$\dot{y}_b + (\omega - \Delta\dot{\theta}/2)\cos(\omega t - \Delta\theta/2) = -\frac{p}{\epsilon_T}y_b - \frac{q\epsilon_L}{\epsilon_T}y_a, \tag{4.57}$$

$$-x_a\sin(\omega t + \Delta\theta/2) + y_a\cos(\omega t + \Delta\theta/2) + \epsilon_T = 0, \tag{4.58}$$

$$-x_b\sin(\omega t - \Delta\theta/2) + y_b\cos(\omega t - \Delta\theta/2) + \epsilon_T(1 + \gamma_M) = 0. \tag{4.59}$$

The analysis of the equations of motion is simplified by the recognition that there are three important time scales in the problem: (i) a short time scale $T_k = \epsilon_T T_0$ which controls the rate of relaxation of the spring, (ii) an intermediate time scale $T_0 = 6\pi\eta R^3/M_a$ that controls the period of the isolated balls, and (iii) a long time scale T_s that characterizes the time for phaselocking to develop; note that $T_k \ll T_0 \ll T_s$. Assume ω, $\Delta\theta$ and $\Delta\dot{\theta}$ change very slowly so that they are only the functions of T_s. Therefore, x_a, y_a, x_b and y_b

can be solved analytically from Eqn. (4.54)-(4.57). These four equations can be written as

$$\begin{pmatrix} \dot{x}_a \\ \dot{x}_b \\ \dot{y}_a \\ \dot{y}_b \end{pmatrix} + \begin{pmatrix} \frac{p}{\epsilon_T} & \frac{2q\epsilon_L}{\epsilon_T} & 0 & 0 \\ \frac{2q\epsilon_L}{\epsilon_T} & \frac{p}{\epsilon_T} & 0 & 0 \\ 0 & 0 & \frac{p}{\epsilon_T} & \frac{q\epsilon_L}{\epsilon_T} \\ 0 & 0 & \frac{q\epsilon_L}{\epsilon_T} & \frac{p}{\epsilon_T} \end{pmatrix} \begin{pmatrix} x_a \\ x_b \\ y_a \\ y_b \end{pmatrix} = \begin{pmatrix} (\omega + \Delta\dot{\theta}/2)\sin(\omega t + \Delta\theta/2) \\ (\omega - \Delta\dot{\theta}/2)\sin(\omega t - \Delta\theta/2) \\ -(\omega + \Delta\dot{\theta}/2)\cos(\omega t + \Delta\theta/2) \\ -(\omega - \Delta\dot{\theta}/2)\cos(\omega t - \Delta\theta/2) \end{pmatrix},$$

or $\dot{X} + AX = B$, where $X = (x_a, y_a, x_b, y_b)^T$ and A is the coefficients matrix. The eigenvalues of matrix A are $(p \pm q\epsilon_L)/\epsilon_T$ and $(p \pm 2q\epsilon_L)/\epsilon_T$. The corresponding eigenvectors are $\{1, 1, 0, 0\}$, $\{1, -1, 0, 0\}$, $\{0, 0, 1, 1\}$ and $\{0, 0, 1, -1\}$. So we can diagonalize A and solve out X. Substitute x_a, y_a, x_b and y_b into Eqn.(4.58)-(4.59) and integrate Eqn. (4.58)-(4.59) in one period $(0, 2\pi/\omega)$. Notice that the phase difference $\Delta\theta$ and its derivative $\Delta\dot{\theta}$ can be regarded as constants during the time interval $(0, 2\pi/\omega)$. So we have

$$\omega = (p + \frac{3}{2}q\epsilon_L \cos\Delta\theta)(1 + \frac{\gamma_M}{2}), \tag{4.60}$$

$$\Delta\dot{\theta} = -\frac{48p^3 q\epsilon_T\epsilon_L \sin\Delta\theta(1+\gamma_M)}{(2p - 3q\epsilon_L\cos\Delta\theta)^2(2p + 3q\epsilon_L\cos\Delta\theta)} - \gamma_M(p - \frac{3}{2}q\epsilon_L\cos\Delta\theta). \tag{4.61}$$

Through hydrodynamic interaction, the excess torque γ_M applied on one ball is shared between the two balls, which is the origin of the term $\gamma_M/2$ in Eqn. (4.60). The phase maps of Eqn. (4.61) with different γ_M are showed in Fig. (4.11). For small γ_M, there exist one stable and one unstable fixed point. The positions of the fixed points are determined by γ_M. If $\gamma_M = 0$, the unstable fixed point would be π or $-\pi$ and the stable fixed point would be 0. As γ_M increases from 0, the two fixed points will close up to each other. If

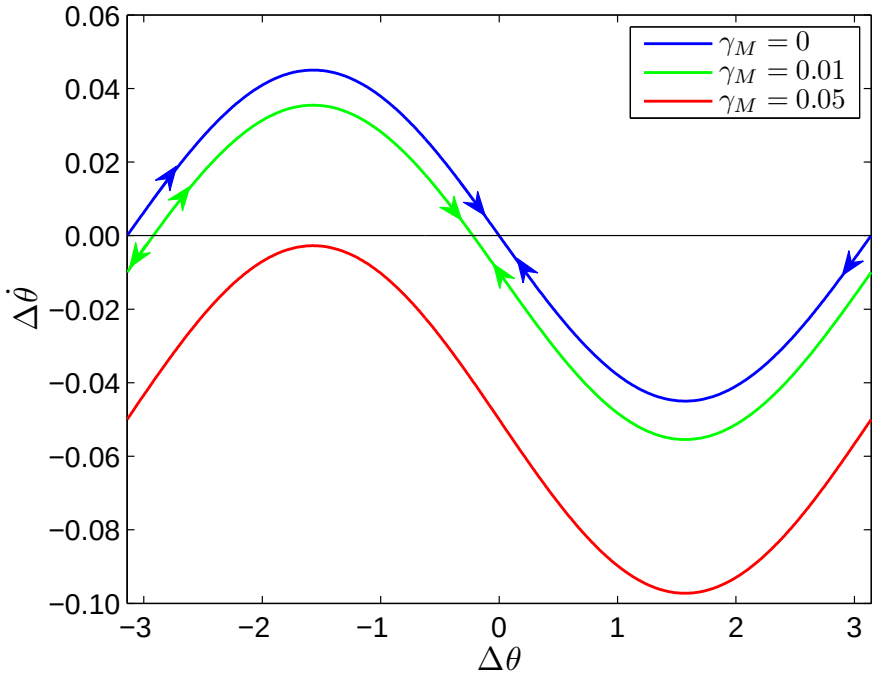

Figure 4.11: The phase maps $\Delta\dot{\theta}$ vs. $\Delta\theta$ for $p = 1$, $\epsilon_T = 0.1$, $\epsilon_L = 0.1$ and different γ_M.

γ_M is beyond some critical value, the fixed points will vanish. That means synchronization cannot be obtained if the two torques differ too much, as shown in Fig. (4.11). This is consistent with the experimental observations in last two sections.

If $\gamma_M = 0$, the velocity fields generated by each ball are in the same direction for $\Delta\theta = 0$, but they are in the opposite direction for $\Delta\theta = \pi$, as shown in Fig. (4.12). So the angular velocity for $\Delta\theta = 0$ is higher than that for independent ball ($h \to \infty$), but the angular velocity for $\Delta\theta = \pi$ is lower. This observation is consistent with Eqn. (4.60).

If the torques are the same ($\gamma_M = 0$), we can get a closed form solution to Eqn. (4.61).

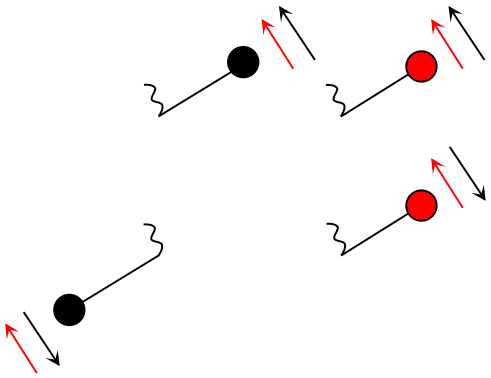

Figure 4.12: The interaction between two balls for $\Delta\theta = 0$ and $\Delta\theta = \pi$. Different colors represent different velocity filed. The arrows indicate the velocity field generated by each ball.

In this case, the governing equations should be

$$\omega = p + \frac{3}{2} q\epsilon_L \cos\Delta\theta, \tag{4.62}$$

$$\Delta\dot{\theta} = -\frac{48p^3 q\epsilon_T\epsilon_L \sin\Delta\theta}{(2p - 3q\epsilon_L\cos\Delta\theta)^2(2p + 3q\epsilon_L\cos\Delta\theta)}. \tag{4.63}$$

There is no explicit solution for $\Delta\theta$ in this case. The corresponding implicit solution is

$$t = \frac{3q\epsilon_L \log[|\frac{\sin(\Delta\theta)}{\sin(\Delta\theta_0)}|] - 2p\log[|\frac{\tan(\Delta\theta/2)}{\tan(\Delta\theta_0/2)}|]}{12pq\epsilon_T\epsilon_L}. \tag{4.64}$$

We can clearly see that the normalized synchronization time T_1/T_0 is proportional to $1/(q\epsilon_T\epsilon_L)$. This means $T_1 \gg T_0$ since $\epsilon_T \ll 1$ and $\epsilon_L \ll 1$. This result shows that our assumption about multiple time scale is valid. The explicit solution can be obtained if we only consider the leading terms of ϵ_L. The governing equations (4.60) and (4.61) are

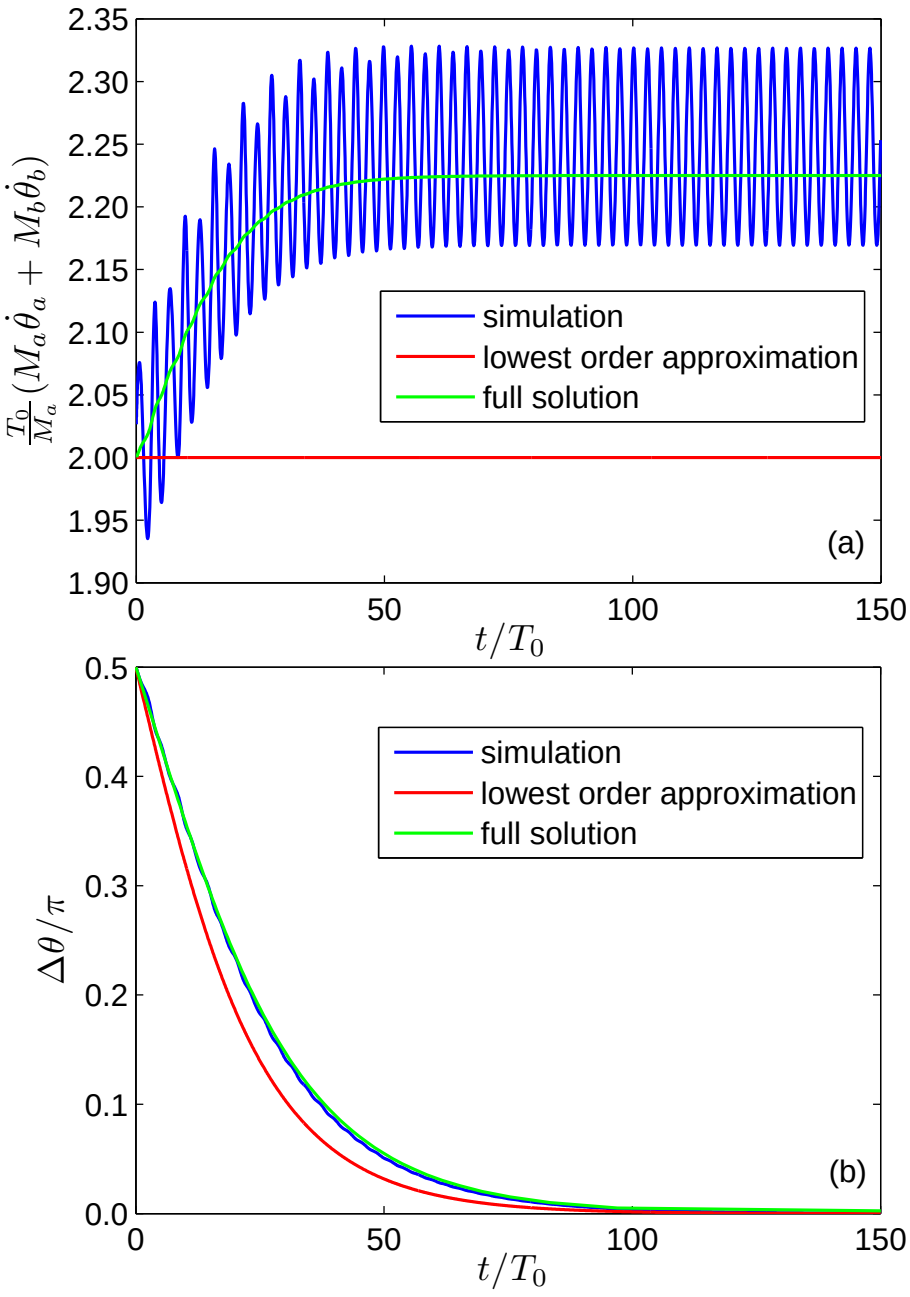

Figure 4.13: Comparison of the analytical solutions with the simulation results for $\gamma_M = 0$, $p = 1$, $\Delta\theta_0 = \pi/2$, $\epsilon_T = 0.1$ and $\epsilon_L = 0.1$. (a) Phase difference vs. dimensionless time; (b) Total dissipation rate vs. dimensionless time.

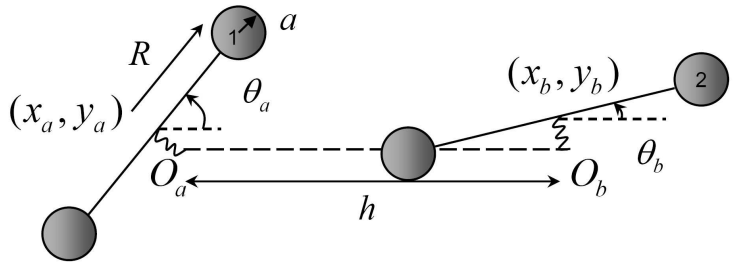

Figure 4.14: Minimal model for symmetric paddles.

reduced to

$$\omega = p, \tag{4.65}$$

$$\Delta\dot{\theta} = -6q\epsilon_T\epsilon_L \sin\Delta\theta. \tag{4.66}$$

The explicit solution to Eqn. (4.66) is

$$\Delta\theta = 2\arctan[\tan(\frac{\Delta\theta_0}{2})e^{-6q\epsilon_T\epsilon_L t}], \tag{4.67}$$

where $\Delta\theta_0$ is the initial phase difference. This result is consistent with reference [66].

The analytical solutions in Eqn. (4.67) and (4.64) are compared with the simulation, as shown in Fig. (4.13). We can see the solution (4.64) is pretty accurate. Furthermore, the torques applied on the paddles are kept constant. So the drag is minimized and the total dissipation rate of the system is maximized during the synchronization process, as shown in Fig (4.13.b).

4.4.2 Symmetric case

Now we consider the symmetric geometry as shown in Fig. (4.14). The symmetric paddles can be modeled as a rotating "dumbell" of two balls of radius a, interacting via the Oseen tensor. The two balls are connected by a rigid shaft, which is driven by moment M and constrained by a spring with spring constant k. The positions of the balls are

$$\mathbf{x}_1 = (-h/2 + x_a + R\cos\theta_a, y_a + R\sin\theta_a), \tag{4.68}$$

$$\mathbf{x}_2 = (-h/2 + x_a - R\cos\theta_a, y_a - R\sin\theta_a), \tag{4.69}$$

$$\mathbf{x}_3 = (h/2 + x_b + R\cos\theta_b, y_b + R\sin\theta_b), \tag{4.70}$$

$$\mathbf{x}_4 = (h/2 + x_b - R\cos\theta_b, y_b - R, \sin\theta_b) \tag{4.71}$$

where $\mathbf{r}_a = (x_a, y_a)$ and $\mathbf{r}_b = (x_b, y_b)$ are the positions of the axes of rotation. h and R are constants which represent the separation of the fixed ends of the springs and the radius of rotation respectively. Here we use a and b to denote the axes of rotation, and use 1, 2, 3 and 4 to denote the balls. The velocities of balls are $\mathbf{v}_i = \dot{\mathbf{x}}_i$. We still use Eqn. (4.35) to describe the dependence of the velocity of the ith ball in terms of the forces acting at each

ball. The balance of the forces and the balance of the torques yield

$$-k_a x_a - F_{1x} - F_{2x} = 0, \tag{4.72}$$

$$-k_a y_a - F_{1y} - F_{2y} = 0, \tag{4.73}$$

$$-k_b x_b - F_{3x} - F_{4x} = 0, \tag{4.74}$$

$$-k_b x_b - F_{3y} - F_{4y} = 0, \tag{4.75}$$

$$(F_{1x} - F_{2x})R\sin\theta_a - (F_{1y} - F_{2y})R\cos\theta_a + M_a = 0, \tag{4.76}$$

$$(F_{3x} - F_{4x})R\sin\theta_b - (F_{3y} - F_{4y})R\cos\theta_b + M_b = 0, \tag{4.77}$$

where F_{ix} and F_{iy} are the x and y components of $\mathbf{F}_i$ ($i = 1, 2, 3$ and 4). k_a and k_b are the spring constants. M_a and M_b are the torques applied on the balls by the motors. Assume the two balls have the same elastic constants and the same torques, e.g. $k_a = k_b = k$ and $M_a = M_b = M$. Define dimensionless parameters $p = R/a$, $q = 3/8$, $\epsilon_T = M/(kR^2)$ and $\epsilon_L = R/h$. Use far field assumption $\epsilon_L \ll 1$ and assume $\epsilon_T \ll 1$. Combine Eqn.(4.35) and Eqn. (4.72)-(4.77), normalize them by length scale R and time scale $T_0 = 6\pi\eta R^3/M$ and

only keep the two lowest terms of ϵ_L, we get the governing equations

$$
\begin{aligned}
\dot{x}_a - \dot{\theta}_a \sin\theta_a &= \frac{p}{\epsilon_T} F_{1x} + \frac{q}{\epsilon_T}\left[(1+\cos^2\theta_a)F_{2x} + \cos\theta_a \sin\theta_a F_{2y}\right] \\
&\quad + \frac{2q}{\epsilon_T}\left[2\epsilon_L\left[1-\epsilon_L(\cos\theta_b - \cos\theta_a)\right]F_{3x} + \epsilon_L^2(\sin\theta_b - \sin\theta_a)F_{3y}\right] \\
&\quad + \frac{2q}{\epsilon_T}\left[2\epsilon_L\left[1+\epsilon_L(\cos\theta_b + \cos\theta_a)\right]F_{4x} - \epsilon_L^2(\sin\theta_b + \sin\theta_a)F_{4y}\right], \\
\dot{x}_a + \dot{\theta}_a \cos\theta_a &= \frac{p}{\epsilon_T} F_{1y} + \frac{q}{\epsilon_T}\left[\cos\theta_a \sin\theta_a F_{2x} + (1+\sin^2\theta_a)F_{2y}\right] \\
&\quad + \frac{2q}{\epsilon_T}\left[\epsilon_L\left[1-\epsilon_L(\cos\theta_b - \cos\theta_a)\right]F_{3y} + \epsilon_L^2(\sin\theta_b - \sin\theta_a)F_{3x}\right]. \\
&\quad + \frac{2q}{\epsilon_T}\left[\epsilon_L\left[1+\epsilon_L(\cos\theta_b + \cos\theta_a)\right]F_{4y} - \epsilon_L^2(\sin\theta_b + \sin\theta_a)F_{4x}\right], \\
\dot{x}_a + \dot{\theta}_a \sin\theta_a &= \frac{p}{\epsilon_T} F_{2x} + \frac{q}{\epsilon_T}\left[(1+\cos^2\theta_a)F_{1x} + \cos\theta_a \sin\theta_a F_{1y}\right] \\
&\quad + \frac{2q}{\epsilon_T}\left[2\epsilon_L\left[1-\epsilon_L(\cos\theta_b + \cos\theta_a)\right]F_{3x} + \epsilon_L^2(\sin\theta_b + \sin\theta_a)F_{3y}\right]. \\
&\quad + \frac{2q}{\epsilon_T}\left[2\epsilon_L\left[1-\epsilon_L(-\cos\theta_b + \cos\theta_a)\right]F_{4x} + \epsilon_L^2(-\sin\theta_b + \sin\theta_a)F_{4y}\right], \\
\dot{x}_a - \dot{\theta}_a \cos\theta_a &= \frac{p}{\epsilon_T} F_{2y} + \frac{q}{\epsilon_T}\left[\cos\theta_a \sin\theta_a F_{1x} + (1+\sin^2\theta_a)F_{1y}\right] \\
&\quad + \frac{2q}{\epsilon_T}\left[\epsilon_L\left[1-\epsilon_L(\cos\theta_b + \cos\theta_a)\right]F_{3y} + \epsilon_L^2(\sin\theta_b + \sin\theta_a)F_{3x}\right]. \\
&\quad + \frac{2q}{\epsilon_T}\left[\epsilon_L\left[1-\epsilon_L(\cos\theta_a - \cos\theta_b)\right]F_{4y} + \epsilon_L^2(\sin\theta_a - \sin\theta_b)F_{4x}\right], \quad (4.78)
\end{aligned}
$$

and

$$
\begin{aligned}
\dot{x}_b - \dot{\theta}_b \sin\theta_b &= \frac{p}{\epsilon_T} F_{3x} + \frac{q}{\epsilon_T}\left[(1+\cos^2\theta_b)F_{4x} + \cos\theta_b \sin\theta_b F_{4y}\right] \\
&\quad + \frac{2q}{\epsilon_T}\left[2\epsilon_L\left[1-\epsilon_L(\cos\theta_b - \cos\theta_a)\right]F_{1x} + \epsilon_L^2(\sin\theta_b - \sin\theta_a)F_{1y}\right] \\
&\quad + \frac{2q}{\epsilon_T}\left[2\epsilon_L\left[1-\epsilon_L(\cos\theta_b + \cos\theta_a)\right]F_{2x} + \epsilon_L^2(\sin\theta_b + \sin\theta_a)F_{2y}\right], \\
\dot{x}_b + \dot{\theta}_b \cos\theta_b &= \frac{p}{\epsilon_T} F_{3y} + \frac{q}{\epsilon_T}\left[\cos\theta_b \sin\theta_b F_{4x} + (1+\sin^2\theta_b)F_{4y}\right] \\
&\quad + \frac{2q}{\epsilon_T}\left[\epsilon_L\left[1-\epsilon_L(\cos\theta_b - \cos\theta_a)\right]F_{1y} + \epsilon_L^2(\sin\theta_b - \sin\theta_a)F_{1x}\right] \\
&\quad + \frac{2q}{\epsilon_T}\left[\epsilon_L\left[1-\epsilon_L(\cos\theta_b + \cos\theta_a)\right]F_{2y} + \epsilon_L^2(\sin\theta_b + \sin\theta_a)F_{2x}\right], \\
\dot{x}_b + \dot{\theta}_b \sin\theta_b &= \frac{p}{\epsilon_T} F_{4x} + \frac{q}{\epsilon_T}\left[(1+\cos^2\theta_b)F_{3x} + \cos\theta_b \sin\theta_b F_{3y}\right] \\
&\quad + \frac{2q}{\epsilon_T}\left[2\epsilon_L\left[1+\epsilon_L(\cos\theta_b + \cos\theta_a)\right]F_{1x} - \epsilon_L^2(\sin\theta_b + \sin\theta_a)F_{1y}\right] \\
&\quad + \frac{2q}{\epsilon_T}\left[2\epsilon_L\left[1-\epsilon_L(-\cos\theta_b + \cos\theta_a)\right]F_{2x} + \epsilon_L^2(-\sin\theta_b + \sin\theta_a)F_{2y}\right], \\
\dot{x}_b - \dot{\theta}_b \cos\theta_b &= \frac{p}{\epsilon_T} F_{4y} + \frac{q}{\epsilon_T}\left[\cos\theta_b \sin\theta_b F_{3x} + (1+\sin^2\theta_b)F_{3y}\right] \\
&\quad + \frac{2q}{\epsilon_T}\left[\epsilon_L\left[1+\epsilon_L(\cos\theta_b + \cos\theta_a)\right]F_{1y} - \epsilon_L^2(\sin\theta_b + \sin\theta_a)F_{1x}\right] \\
&\quad + \frac{2q}{\epsilon_T}\left[\epsilon_L\left[1-\epsilon_L(\cos\theta_a - \cos\theta_b)\right]F_{2y} + \epsilon_L^2(\sin\theta_a - \sin\theta_b)F_{2x}\right]. \quad (4.79)
\end{aligned}
$$

To simplify the problem further, we use the same method as in asymmetric case. Define average phase angle $\bar{\theta} = \frac{1}{2}(\theta_a + \theta_b) = \omega t$ and phase difference $\Delta\theta = \theta_a - \theta_b$, where $\omega = \frac{d\bar{\theta}}{dt}$ is the average rotation speed. Similarly, as in the asymmetric case, we have three important time scales as the asymmetric case: (i) a short time scale $T_k = \epsilon_T T_0$ which controls the rate of relaxation of the spring, (ii) an intermediate time scale $T_0 = 6\pi\eta R^3/M_a$ that controls the period of the isolated balls, and (iii) a long time scale T_s that characterizes the time for phaselocking to develop; note that $T_k \ll T_0 \ll T_s$. Assume ω, $\Delta\theta$ and $\Delta\dot{\theta}$ change very

slowly so that they are only the functions of T_s. Substitute the Eqn. (4.72)-(4.75) to Eqn. (4.78) and (4.79). Introduce some new variables $\Delta F_{ax} = F_{1x} - F_{2x}$, $\Delta F_{ay} = F_{1y} - F_{2y}$, $\Delta F_{bx} = F_{3x} - F_{4x}$ and $\Delta F_{by} = F_{3y} - F_{4y}$. After simplification, we have

$$
\begin{aligned}
& -2(\omega + \Delta\dot{\theta}/2)\sin(\omega t + \Delta\theta/2) \\
= \; & \frac{p}{\epsilon_T}\Delta F_{ax} + \frac{q}{\epsilon_T}\left[-(1+\cos^2(\omega t + \Delta\theta/2))\Delta F_{ax} - \cos(\omega t + \Delta\theta/2)\sin(\omega t + \Delta\theta/2)\Delta F_{ay}\right] \\
& + \frac{4q\epsilon_L^2}{\epsilon_T}\left[-2\cos(\omega t + \Delta\theta/2)x_b + \sin(\omega t + \Delta\theta/2)y_b\right], \\
& 2(\omega + \Delta\dot{\theta}/2)\cos(\omega t + \Delta\theta/2) \\
= \; & \frac{p}{\epsilon_T}\Delta F_{ay} + \frac{q}{\epsilon_T}\left[-\cos(\omega t + \Delta\theta/2)\sin(\omega t + \Delta\theta/2)\Delta F_{ax} - (1+\sin^2(\omega t + \Delta\theta/2))\Delta F_{ay}\right] \\
& + \frac{4q\epsilon_L^2}{\epsilon_T}\left[-\cos(\omega t + \Delta\theta/2)y_b + \sin(\omega t + \Delta\theta/2)x_b\right], \\
& -2(\omega - \Delta\dot{\theta}/2)\sin(\omega t - \Delta\theta/2) \\
= \; & \frac{p}{\epsilon_T}\Delta F_{bx} + \frac{q}{\epsilon_T}\left[-(1+\cos^2(\omega t - \Delta\theta/2))\Delta F_{bx} - \cos(\omega t - \Delta\theta/2)\sin(\omega t - \Delta\theta/2)\Delta F_{by}\right] \\
& + \frac{4q\epsilon_L^2}{\epsilon_T}\left[2\cos(\omega t - \Delta\theta/2)x_a - \sin(\omega t - \Delta\theta/2)y_a\right], \\
& 2(\omega - \Delta\dot{\theta}/2)\cos(\omega t - \Delta\theta/2) \\
= \; & \frac{p}{\epsilon_T}\Delta F_{by} + \frac{q}{\epsilon_T}\left[-\cos(\omega t - \Delta\theta/2)\sin(\omega t - \Delta\theta/2)\Delta F_{bx} - (1+\sin^2(\omega t - \Delta\theta/2))\Delta F_{by}\right] \\
& + \frac{4q\epsilon_L^2}{\epsilon_T}\left[\cos(\omega t - \Delta\theta/2)y_a - \sin(\omega t - \Delta\theta/2)x_a\right], \qquad (4.80)
\end{aligned}
$$

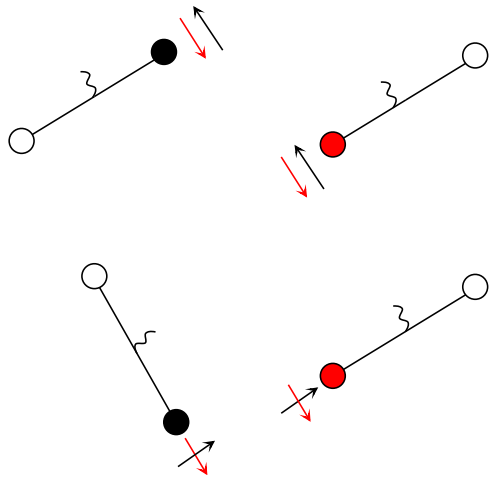

Figure 4.15: The hydrodynamic interaction between four balls for $\Delta\theta = 0$ and $\Delta\theta = \pi/2$. Different colors represent different velocity filed. The arrows indicate the velocity field generated by each ball.

and

$$
\begin{aligned}
2\dot{x}_a &= -\frac{p}{\epsilon_T}x_a - \frac{q}{\epsilon_T}\left[(1+\cos^2(\omega t+\Delta\theta/2))x_a + \cos(\omega t+\Delta\theta/2)\sin(\omega t+\Delta\theta/2)y_a\right] \\
&\quad + \frac{4q\epsilon_L}{\epsilon_T}\left[-2x_b - 2\epsilon_L\cos(\omega t-\Delta\theta/2)\Delta F_{bx} + \epsilon_L\sin(\omega t-\Delta\theta/2)\Delta F_{by}\right], \\
2\dot{y}_a &= -\frac{p}{\epsilon_T}y_a - \frac{q}{\epsilon_T}\left[\cos(\omega t+\Delta\theta/2)\sin(\omega t+\Delta\theta/2)x_a + (1+\sin^2(\omega t+\Delta\theta/2))y_a\right] \\
&\quad + \frac{4q\epsilon_L}{\epsilon_T}\left[-y_b - \epsilon_L\cos(\omega t-\Delta\theta/2)\Delta F_{by} + \epsilon_L\sin(\omega t-\Delta\theta/2)\Delta F_{bx}\right], \\
2\dot{x}_b &= -\frac{p}{\epsilon_T}x_b - \frac{q}{\epsilon_T}\left[(1+\cos^2(\omega t-\Delta\theta/2))x_b + \cos(\omega t-\Delta\theta/2)\sin(\omega t-\Delta\theta/2)y_b\right] \\
&\quad + \frac{4q\epsilon_L}{\epsilon_T}\left[-2x_a + 2\epsilon_L\cos(\omega t+\Delta\theta/2)\Delta F_{ax} - \epsilon_L\sin(\omega t+\Delta\theta/2)\Delta F_{ay}\right], \\
2\dot{y}_b &= -\frac{p}{\epsilon_T}y_b - \frac{q}{\epsilon_T}\left[\cos(\omega t-\Delta\theta/2)\sin(\omega t-\Delta\theta/2)x_b + (1+\sin^2(\omega t-\Delta\theta/2))y_b\right] \\
&\quad + \frac{4q\epsilon_L}{\epsilon_T}\left[-y_a + \epsilon_L\cos(\omega t+\Delta\theta/2)\Delta F_{ay} - \epsilon_L\sin(\omega t+\Delta\theta/2)\Delta F_{ax}\right]. \qquad (4.81)
\end{aligned}
$$

ΔF_{ax}, ΔF_{ay}, ΔF_{bx} and ΔF_{by} can be solve out directly from Eqn. (4.80). Substituting them into Eqn. (4.81), we get four ODEs about variables x_a, y_a, x_b and y_b. The ODEs

can be written as

$$\dot{X} = (A + \epsilon_L B + \epsilon_L^2 C + \epsilon_L^4 D)X + \epsilon_L^2 E \tag{4.82}$$

where $X = (x_a, y_a, x_b, y_b)^T$ and A, B, C, D and E are the coefficients matrixes. Assume $X = X_0 + \epsilon_L X_1 + \epsilon_L^2 X_2 + \epsilon_L^3 X_3 + ...$ and substitute X into Eqn. (4.82), we get the iterative formula

$$\dot{X}_0 = AX_0 \tag{4.83}$$

$$\dot{X}_1 = AX_1 + BX_0 \tag{4.84}$$

$$\dot{X}_2 = AX_2 + BX_1 + CX_0 + E \tag{4.85}$$

$$\dot{X}_3 = AX_3 + BX_2 + CX_1 \tag{4.86}$$

If we neglect the transient solution, then $X_0 = X_1 = 0$. The last two equations can be solved with the same method introduced in last section. The final solution would be

$$X = \epsilon_L^2 X_2 + \epsilon_L^3 X_3. \tag{4.87}$$

Substitute x_a, y_a, x_b and y_b into Eqn.(4.76)-(4.77) and integrate Eqn. (4.76)-(4.77) in one period $(0, 2\pi/\omega)$. The governing equations are

$$\omega = \frac{1}{2}(p - q) - \frac{\epsilon_L^4 q^2 (34p + 51q + 12q\cos(2\Delta\theta))}{2(p+q)(p+2q)} \tag{4.88}$$

$$\Delta\dot{\theta} = \epsilon_T \epsilon_L^5 \left[A + B\cos(2\Delta\theta)\right] \sin(2\Delta\theta) \tag{4.89}$$

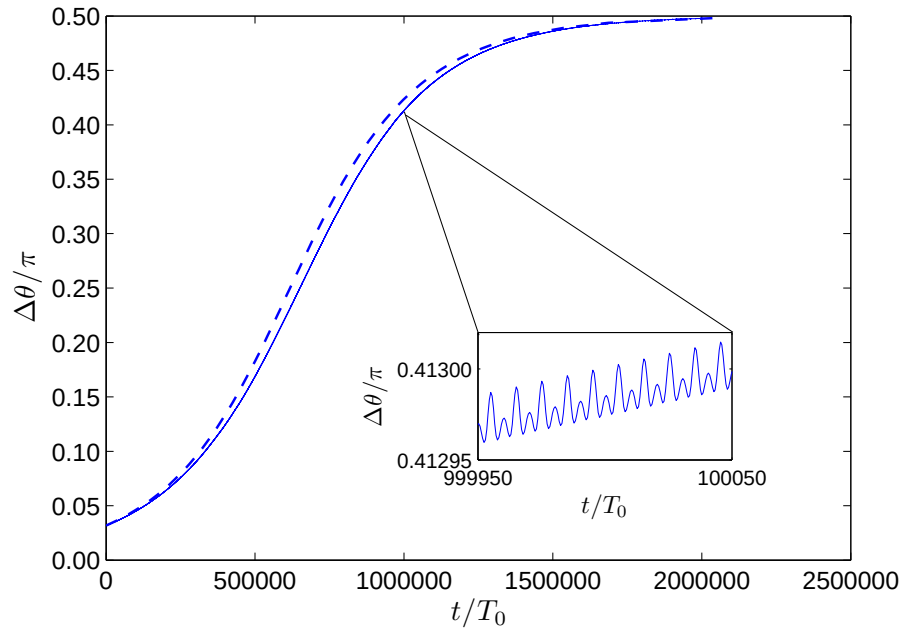

Figure 4.16: Comparison of the analytical solutions with the simulation results for $p = 1$, $\Delta\theta_0 = 0.1$, $\epsilon_T = 0.1$ and $\epsilon_L = 0.08$. Dashed line represents the analytical solution.

The solution to Eqn.(4.89) is

$$t = \frac{-(A+B)\log(\frac{\cos^2\Delta\theta}{\cos^2\Delta\theta_0}) + 2B\log(\frac{A+B\cos(2\Delta\theta)}{A+B\cos(2\Delta\theta_0)}) + (A-B)\log(\frac{\sin^2\Delta\theta}{\sin^2\Delta\theta_0})}{4(A^2-B^2)\epsilon_T\epsilon_L^5} \quad (4.90)$$

where

$$A = \frac{6q^3(p-q)(96p^3+464p^2q+752pq^2+412q^3)}{(p+q)^3(p+2q)^3} \quad (4.91)$$

$$B = \frac{54q^5(p-q)(2p+3q)}{(p+q)^3(p+2q)^3} \quad (4.92)$$

The leading order of x_a, y_a, x_b and y_b is ϵ_L^2 since the dumbbells are force dipoles for $\epsilon_L \ll 1$. This means the second lower order of ΔF_{ax}, ΔF_{ay}, ΔF_{bx} and ΔF_{by} is ϵ_L^4 from Eqn. (4.80). This explains why there is a ϵ_L^4 term in Eqn. (4.88). The second lower order of x_a,

y_a, x_b and y_b is ϵ_L^3, as shown in Eqn. (4.87). This is the reason that $\Delta\dot{\theta}$ is proportional to ϵ_L^5 in Eqn. (4.88).

The phase map of Eqn. (4.89) is quite similar with that of Eqn. (4.61) except that the stable fixed point is $\Delta\theta = \pi/2$ and unstable fixed point is $\Delta\theta = 0$. Here we only consider $0 \leq \Delta\theta < \pi$ due to the symmetry. The two closet balls have the strongest interaction. So the synchronization behavior is mainly determined by them. The velocity fields generated by the two balls are in the different direction for $\Delta\theta = 0$, but they are perpendicular to each other for $\Delta\theta = \pi/2$ as shown in Fig. (4.15). So the angular velocity for $\Delta\theta = 0$ is lower than that for $\Delta\theta = \pi/2$. This observations is consistent with Eqn. (4.88). This means the total dissipation rate of the system is still maximized for symmetric case. The normalized synchronization time T_1/T_0 is proportional to $\frac{1}{\epsilon_T \epsilon_L^5}$, which means the synchronization time is very sensitive to the separation between the two paddles. This is consistent with our experimental observations. The analytical solution in Eqn. (4.90) is also consistent with the simulation, as shown in Fig. (4.16).

4.5 Conclusion

A model problem that captures the essential features of hydrodynamic interactions between flexible cilia and bacterial flagella was investigated experimentally, computationally and theoretically. A pair of rigid paddles (symmetric or asymmetric) are rotated in close proximity, coupled by the induced flow of the surrounding viscous fluid. An inflexible system does not synchronize. However, if a small degree of flexibility is introduced, synchronization is observed with the paddles settling to a state that minimized their hydrodynamic

interactions. Numerical simulations using regularized stokeslet techniques was consistent with experimental data perfectly. The theoretical model explained all the experimental observations and provided more insight into the mechanism of hydrodynamic synchronization.

Bibliography

[1] Lipid bilayer. *http://en.wikipedia.org/wiki/Cell_membrane.*

[2] P. Nassoy J. Prost P. Bassereau A. Roux, D. Cuvelier and B. Goud. Role of curvature and phase transition in lipid sorting and fission of membrane tubules. *EMBO J.*, **24**:1537, 2005.

[3] T. Bretschneider M. Schleicher A. Schirenbeck, R. Arasada and J. Faix. Formins and vasps may co-operate in the formation of filopodia. *Biochem. Soc. Trans.*, **33**:1256, 2005.

[4] W. Wang A. Tian, C. Johnson and T. Baumgart. Line tension at fluid membrane domain boundaries measured by micropipette aspiration. *Phys. Rev. Lett.*, **98**:208102, 2007.

[5] G. P. Alexander and J. M. Yeomans. Dumb-bell swimmers. *Euro. Phys. Lett.*, 83:34006, 2008.

[6] D. A. Gagnon T. R. Powers B. Qian, H. Jiang and K. S. Breuer. Minimal model for hydrodynamic synchronization. *submitted to Phys. Rev. Lett.*, 2009.

[7] T. Baumgart, S. T. Hess, and W. W. Webb. Imaging coexisting fluid domains in biomembrane models coupling curvature and line tension. *Nature*, **425**:821–24, 2003.

[8] Matthew Bennett, Michael F. Schatz, Heidi Rockwood, and Kurt Wiesenfeld. Huygens's clocks. *Proc. R. Soc. Lond. A*, 458:563–579, 2002.

[9] Matthew Bennett, Michael F. Schatz, Heidi Rockwood, and Kurt Wiesenfeld. Huygens's clocks. *Proc. R. Soc. Lond. A*, 458:563–579, 2002.

[10] M. J. Bowick, D. R. Nelson, and A. Travesset. Interacting topological defects on frozen topographies. *Phys. Rev. B*, **62**:8738, 2000.

[11] M. J. Bowick, D. R. Nelson, and A. Travesset. Curvature-induced defect unbinding in toroidal geometries. *Phys. Rev. B*, **69**:041102, 2004.

[12] P. G. Higgs C. M. Chen and F. C. Mackintosh. Theory of fission for two-component lipid vesicles. *Phys. Rev. Lett.*, **79**:1579, 1997.

[13] P.B. Canham. The minimum energy of bending as a possible explanation of the biconcave shape of the human red blood cell. *J. Theor. Biol.*, **26**:61–81, 1970.

[14] R. Cortez. The method of regularized Stokeslets. *SIAM J. Sci. Comput.*, **23**:1204–1225, 2001.

[15] P. Bassereau D. Cuvelier, I. Derényi and P. Nassoy. Coalescence of membrane tethers: Experiments, theory, and applications. *Biophys. J.*, **88**:2714, 2005.

[16] F. David. In D. R. Nelson, T. Piran, and S. Weinberg, editors, *Statistical Mechanics of Membranes and Surfaces: Jerusalem Winter School for Theoretical Physics*. World Scientific, Singapore, 1989.

[17] P. G. de Gennes and J. Prost. *The Physics of Liquid Crystals*. Oxford University Press, Oxford, 2nd edition, 1995.

[18] J. Derganc, A. A. Mironov, and S. Svetina. Physical factors that affect the number and size of Golgi cisternae. *Traffic*, **7**:85–96, 2006.

[19] H.-G. Döbereiner, E. Evans, M. Kraus, U. Seifert, and M. Wortis. Mapping vesicle shapes into the phase diagram: a comparison of experiment and theory. *Phys. Rev. E*, **55**:4458, 1997.

[20] H.-G. Döbereiner, O. Selchow, and R. Lipowsky. Spontaneous curvature of fluid vesicles induced by trans-bilayer sugar symmetry. *Eur. Biophys. J.*, **28**:174, 1999.

[21] M. Doi and S.F. Edwards. *The theory of polymer dynamics*. Oxford University Press, Oxford, 1986.

[22] C.R. Safinya R.J. Plano E.B. Sirota, G.S. Smith and N.A. Clark. X-ray scattering studies of aligned, stacked surfactant membranes. *Science*, **242**:1406, 1988.

[23] N. Sciaky *et al.* Golgi tubule traffic and the effects of brefeldin A visualized in living cells. *J. Cell Bio.*, **139**:5, 1997.

[24] R. M. L. Evans. Phase diagrams for deformable toroidal and spherical surfaces with intrinsic orientational order. *J. Phys. II France*, **5**:507, 1995.

[25] L. J. Fauci. Interaction of oscillating filaments - A computational study. *J. Comp. Phys.*, 86:294–313, 1990.

[26] V. A. Frolov, V. A. Lizunov, A. Ya. Dunina-Barkovskaya, A. V. Samsonov, and J. Zimmerberg. Shape bistability of a membrane neck: a toggle switch to control vesicle content release. *Proc. Natl. Acad. Sci. USA*, **100**:8698–8703, 2003.

[27] I. Derényi D. Frenkel G. Koster, A. Cacciuto and M. Dogterom. Force barriers for membrane tube formation. *Phys. Rev. Lett.*, **94**:068101, 2005.

[28] J. Gray. *Ciliary movement.* Cambridge University Press, Cambridge, U.K., 1928.

[29] S. Gueron, K. Levit-Gurevich, N. Liron, and J. J. Blum. Cilia internal mechanism and metachronal coordination as the result of hydrodynamical coupling. *Proc. Natl. Acad. Sci. USA*, 94:6001–6006, 1997.

[30] S. Gueron and N. Liron. Ciliary motion modeling, and dynamic multicilia interactions,. *Biophys. J.*, **63**:1045–1058, 1992.

[31] B. Guirao and J. F. Joanny. Spontaneous creation of macroscopic flow and metachronal waves in an array of cilia. *Biophys. J.*, 92:1900–1917, 2007.

[32] R. A. Pelcovits H. Jiang, G. Huber and T. R. Powers. Vesicle shape, molecular tilt, and the suppression of necks. *Phys. Rev. E*, **76**:031908, 2007.

[33] V. Heinrich and R. E. Waugh. A piconewton force transducer and its application to measurement of the bending stiffness of phospholipid membranes. *Ann. Biomed. Eng.*, **24**:595, 1996.

[34] W. Helfrich. Elastic properties of lipid bilayers: theory and possible experiments. *Z. Naturforsh.*, **28c**:693, 1973.

[35] J.L.L. Higdon. The generation of feeding currents by flagellar motions. *J. Fluid Mech.*, **94**:305, 1979.

[36] J.L.L. Higdon. A hydrodynamic analysis of flagellar propulsion. *J. Fluid Mech.*, **90**:685–711, 1979.

[37] F. Julicher I. Derényi and J. Prost. Formation and interaction of membrane tubes. *Phys. Rev. Lett.*, **88**:238101, 2002.

[38] M. M. van Duijn A. Czövek M. Dogterom I. Derényi, G. Koster and J. Prost. in *controlled nanoscale motion* edited by h. linke and a. mansson (springer- verlag, berlin, 2007) vol. 711 of *lecture notes in physics*, pp. 141c159.

[39] A. Roux M. B. Amar J. M. Allain, C. Storm and J. F. Joanny. Fission of a multiphase membrane tube. *Phys. Rev. Lett.*, **93**:158104, 2004.

[40] G. Strouse J. Yuan, S. Hira and L.S. Hirst. Lipid bilayer discs and banded tubules: Photoinduced lipid sorting in ternary mixtures. *JOURNAL OF THE AMERICAN CHEMICAL SOCIETY*, **130**:2067, 2008.

[41] H. Jiang and T. R. Powers. Curvature-driven lipid sorting in a membrane tubule. *Phys. Rev. Lett.*, **101**:018103, 2008.

[42] F. Jülicher and R. Lipowsky. Domain-induced budding of vesicles. *Phys. Rev. Lett.*, **26**:2964, 1993.

[43] F. Jülicher and R. Lipowsky. Shape transformations of vesicles with intramembrane domains. *Phys. Rev. E*, 53:2670, 1996.

[44] D. Toomre K. Simons. Lipid rafts and signal transduction. *Nat. Rev. Mol. Cell Biol.*, 1:31–39, 2000.

[45] R. D. Kamien. The geometry of soft materials: a primer. *Rev. Mod. Phys.*, **74**:953–971, 2002.

[46] J.B. Keller and S.I. Rubinow. Slender body theory for viscous flow. *J. Fluid Mech.*, **75**:705–714, 1976.

[47] M. J. Kim and T. R. Powers. *Phys. Rev. E*, 69:061910, 2004.

[48] M. C. Lagomarsino, B. Bassetti, and P. Jona. Rowers coupled hydrodynamically. Modeling possible mechanisms for the cooperation of cilia. *Europ. Phys. J. B*, 26:81–88, 2002.

[49] M. C. Lagomarsino, P. Jona, and B. Bassetti. Metachronal waves for deterministic switching two-state oscillators with hydrodynamic interaction. *Phys. Rev. E*, 68:021908, 2003.

[50] E. Lauga and D. Bartolo. No many-scallop theorem: Collective locomotion of reciprocal swimmers. *Phys. Rev. E*, 78:030901, 2008.

[51] S. Leibler and D. Andelman. Ordered and curved meso-structures in membranes and amphiphilic films. *J. Phys.*, **48**:2013, 1987.

[52] P. Lenz and A. Ryskin. Collective effects in ciliar arrays. *Phys. Biol.*, 3:285–294, 2006.

[53] J. Lighthill. Flagellar hydrodynamics. *SIAM Review*, **18**:161–230, 1976.

[54] J. Lighthill. Helical distribution of stokeslets. *J. Eng. Math.*, **30**:35–78, 1996.

[55] R. Lipowsky. Budding of membranes induced by intramembrane domains. *J. Phys. II (France)*, **2**:1825, 1992.

[56] C.P. Lowe. Dynamics of filaments: modelling the dynamics of driven microfilaments. *Phil. Trans. R. Soc. Lond. B*, **358**:1543–1550, 2003.

[57] T. C. Lubensky and J. Prost. Orientational order and vesicle shape. *J. Phys. II France*, **2**:371, 1992.

[58] H. Machemer. Ciliary action and the origin of metachrony in *Paramecium*: effects of increased viscosity. *J. Exp. Biol.*, **57**:239, 1972.

[59] F. C. MacKintosh and T. C. Lubensky. Orientational order, topology, and vesicle shapes. *Phys. Rev. Lett.*, **67**:1169, 1991.

[60] H. T. McMahon and J. L. Gallop. Membrane curvature and mechanisms of dynamic cell membrane remodelling. *Nature*, **438**:590, 2005.

[61] G. V. Meer and H. Sprong. Membrane lipids and vesicular traffic. *Curr. Opin. Cell Biol.*, **16**:373, 2004.

[62] R. S. Millman and G. D. Parker. *Elements of differential geometry.* Prentice Hall, New York, 1977.

[63] O. Mouritsen. *Life as a matter of fat: the emerging science of lipidomics.* Springer-Verlag, Berlin, 2005.

[64] S. Mukherjee and F. R. Maxfield. Role of membrane organization and membrane domains in endocytic lipid trafficking. *Traffic*, **1**:203, 2000.

[65] P. Nelson and T. Powers. Renormalization of chiral couplings in tilted bilayer membranes. *J. Phys. II France*, **3**:1535, 1993.

[66] T. Niedermayer, B. Eckhardt, and P. Lenz. Synchronization, phase locking, and metachronal wave formation in ciliary chains. *Chaos*, 18:037128, 2008.

[67] S. Nonaka, Y. Tanaka, S. Takeda, A. Harada, Y. Kanai, M. Kido, and N. Hirokawa. Randomization of left-right asymmetry due to loss of nodal cilia generating leftward flow of extraembryonic fluid in mice lacking KIF3b motor protein. *Cell*, **95**:829, 1998.

[68] A. Pikovsky, M. Rosenblum, and J. Kurths. *Synchronization. A universal concept in nonlinear science*. Cambridge University Press, Cambridge, 2001.

[69] T. Powers and P. Nelson. Fluctuating membranes with tilt order. *J. Phys. II (France)*, **5**:1671, 1995.

[70] T.R. Powers, G. Huber, and R.E. Goldstein. Fluid-membrane tethers: elastic boundary layers and minimal surfaces. *Phys. E*, 65:041901, 2002.

[71] L. Fauci R. Cortez and A. Medovikov. The method of regularized stokeslets in three dimensions: Analysis, validation and applications to helical swimming. *Physics of Fluids*, **17**:031504, 2005.

[72] C. Yu R. Parthasarathy and J. T. Groves. Curvature-modulated phase separation in lipid bilayer membranes. *Langmuir*, **22**:5095, 2006.

[73] M. Reichert and H. Stark. *Eur. Phys. J. E*, 17:493, 2005.

[74] Ingmar H. Riedel, Karsten Kruse, and Jonathon Howard. *Science*, 309:300, 2005.

[75] Sarasij R. C., S. Mayor, and M. Rao. Chirality-induced budding: a raft-mediated mechanism for endocytosis and morphology of caveolae? *Biophys. J.*, **92** :3140, 2007.

[76] Sarasij R. C. and M. Rao. Tilt texture domains on a membrane and chirality induced budding. *Phys. Rev. Lett.*, **88**:088101–1, 2002.

[77] U. Seifert. Curvature-induced lateral phase segregation in two-component vesicles. *Phys. Rev. Lett.*, **70**:1335, 1993.

[78] U. Seifert. Configurations of fluid membranes and vesicles. *Adv. Phys.*, **46**:13, 1997.

[79] Udo Seifert, Karin Berndl, and Reinhard Lipowsky. Shape transformation of vesicles: phase diagram for spontaneous-curvature and bilayer-coupling models. *Phys. Rev. A*, **44**:1182, 1991.

[80] J. V. Selinger, F. C. MacKintosh, and J. M. Schnur. Theory of cylindrical tubules and helical ribbons of chiral lipid membranes. *Phys. Rev.*, E **53**:3804, 1996.

[81] L. F. Shampine, I. Gladwell, and S. Thompson. *Solving ODE's with MATLAB*. Cambridge University Press, New York, 2003.

[82] M. A. Sleigh, ed. *Cilia and flagella*. Academic Press, London, 1974.

[83] G. Smith, E. Sirota, C. Safinya, and N. Clark. Structure of the l_β phases in a hydrated phosphatidylcholine multimembrane. *Phys. Rev. Lett.*, **60**:813, 1988.

[84] G.S. Smith, E.B. Sirota, C.R. Safinya, R.J. Plano, and N.A. Clark. X-ray structural studies of freely suspended ordered hydrated dmpc multimembrane films. *J. Chem. Phys.*, **92**:4519, 1990.

[85] S. S. Suarez and A. A. Pacey. Sperm transport in the female reproductive tract. *Human Reprod. Update*, 12:23–37, 2006.

[86] S. Svetina and B. Zeks. Bilayer couple hypothesis of red cell shape transformations and osmotic hemolysis. *Biomed. Biochim. Acta*, **42**:86, 1983.

[87] S. Svetina and B. Zeks. Membrane bending energy and shape determination of phospholipid vesicles and red blood cells. *Eur. Biophys. J.*, **17**:101, 1989.

[88] Z. C. Tu and U. Seifert. Concise theory of chiral lipid membranes. *cond-mat:0705.2707v1*, 2007.

[89] S. L. Veatch and S. L. Keller. Organization in lipid membranes containing cholesterol. *Phys. Rev. Lett.*, **89**:268101, 2002.

[90] Andrej Vilfan and Frank Julicher. *Phys. Rev. Lett.*, 96:058102, 2006.

[91] V. Vitelli and D. R. Nelson. Defect generation and deconfinement on corrugated topographies. *Phys. Rev. E*, **70**:051105, 2004.

[92] M. Takashima P. Brecht J. H. Torres Z. Li, B. Anvari and W. E. Brownell. Membrane tether formation from outer hair cells with optical tweezers. *Biophys. J.*, **82**:1386, 2002.

[93] Y. Brechet T. Vicsek A.L. Barabái Z. Néa, E. Ravasz. The sound of many hands clapping. *Nature*, **403**:849, 2000.

[94] Y. Zhao, N. Mahajan, R. Lu, and J. Fang. Liquid-crystal imaging of molecular-tilt ordering in self-assembled lipid tubules. *Proc. Natl. Acad. Sci. USA*, 102:7438–7442, 2005.